

University of Central Florida

**STARS**

---

Graduate Thesis and Dissertation 2023-2024

---

2024

# Next-generation High-performance Virtual Reality and Augmented Reality Light Engines

Zhiyong Yang

*University of Central Florida*



Part of the [Optics Commons](#)

Find similar works at: <https://stars.library.ucf.edu/etd2023>

University of Central Florida Libraries <http://library.ucf.edu>

This Doctoral Dissertation (Open Access) is brought to you for free and open access by STARS. It has been accepted for inclusion in Graduate Thesis and Dissertation 2023-2024 by an authorized administrator of STARS. For more information, please contact [STARS@ucf.edu](mailto:STARS@ucf.edu).

---

## STARS Citation

Yang, Zhiyong, "Next-generation High-performance Virtual Reality and Augmented Reality Light Engines" (2024). *Graduate Thesis and Dissertation 2023-2024*. 107.

<https://stars.library.ucf.edu/etd2023/107>

NEXT-GENERATION HIGH-PERFORMANCE VIRTUAL REALITY AND AUGMENTED  
REALITY LIGHT ENGINES

by

ZHIYONG YANG  
B.S. Chongqing University, 2017  
M.S. University of Michigan, 2019

A dissertation submitted in partial fulfillment of the requirements  
for the degree of Doctor of Philosophy  
in the College of Optics and Photonics  
at the University of Central Florida  
Orlando, Florida

Spring Term  
2024

Major Professor: Shin-Tson Wu

© 2024 Zhiyong Yang

## ABSTRACT

The immersive virtual reality (VR) and the optical see-through augmented reality (AR) are expected to revolutionize human lives in work, education, entertainment, healthcare, spatial computing, and digital twins, just to name a few. Next-generation VR/AR devices should exhibit a wide field-of-view (FoV), crisp image without screen-door effect, high dynamic range, compact form factor and lightweight, and low power consumption. Such demanding requirements pose a significant challenge to traditional direct-view display panels. To address these technical challenges, novel approaches need to be proposed. This dissertation is devoted to developing next-generation high-performance display light engines toward high resolution density, high optical efficiency, wide color gamut, and small form factor. These emerging solutions will fuel the growth and accelerate the widespread applications of VR/AR devices.

In Chapter 2, we propose practical measurement methods to characterize the halo artifacts of miniature light-emitting diode (mini-LED) backlit liquid crystal displays (LCDs). After measuring and characterizing a high dynamic range (HDR) light engine, we propose and develop field sequential color (FSC) LCDs for high-end virtual reality (VR) devices in Chapter 3. Such an FSC LCD can triple the resolution density and optical efficiency via eliminating color filters. To further mitigate the color breakup (CBU), we also propose to combine mini-LEDs with FSC LCDs to enable progressive emission and achieve a higher frame rate ( $\sim 600$  Hz). To quantitatively compare the CBUs corresponding to simultaneous emission, progressive emission, and stencil algorithm, we adopt the CIEDE2000 color difference as a metric. Quantitative simulation results of the CBU indicate that a 600-Hz subframe rate can help mitigate the CBU dramatically.

Micro organic light-emitting diode (micro-OLED) exhibiting high-resolution density and high contrast ratio is another type of display for high-end VR devices. More specifically, white micro-OLED is currently employed because it helps ease the manufacturing difficulty. In Chapter 4, we optimize the layer thicknesses to achieve a maximum efficiency while keeping a decent color gamut. We also push the limit of color gamut toward  $\sim 95\%$  Rec. 2020. Lastly, liquid-crystal-on-silicon (LCoS) offers great potential for achieving high-efficiency and high-resolution waveguide-based AR displays. In Chapter 5, several strategies are proposed and developed to improve the performance of LCoS microdisplays and enable a small pixel size. In Chapter 6, we briefly summarize our major accomplishments.

Keywords: Virtual reality displays; Augmented reality displays; Field sequential color LCD; Micro-OLED; LCoS microdisplay.

To my beloved family.

## ACKNOWLEDGEMENTS

First of all, I would like to thank my thesis advisor, Dr. Shin-Tson Wu, for his long-lasting guidance and care. He always encouraged me to do first-class research that would have a profound impact. His remarkable vision, tremendous wisdom, and rich knowledge taught me how to be a great leader and an outstanding scientist. I always feel so blessed to learn from him and develop a precious friendship where we can share both research and personal life. In addition, I would like to thank Prof. Wu's better half, Cho-Yan Hsieh, for making me feel at home and caring my life and study. When I missed my original hometown and felt alone, her endless care made me feel very warm and moved. Because of that, I treat Orlando as my second hometown. Also, I would like to thank my committee members, Dr. M. G. Moharam, Dr. Patrick L. LiKamWa, and Dr. Yajie Dong. They always gave me instructive feedback on my research and showed their support to my scholarship applications.

My lab partners and collaborators accompany me in the incredible journey by mutual discussions and inspirations. Here, I would like to thank past and present team members, especially Dr. Tao Zhan, Dr. Ziqian He, Dr. Jianghao Xiong, Dr. Kun Yin, Dr. En-Lin Hsiang, Dr. Yannanqi Li, Dr. Junyu Zou, Qian Yang, Zhenyi Luo, Yizhou Qian, Yuqiang Ding, and Jason Adams. As for forming a more comprehensive perspective on display systems, I want to thank Prof. Chih-Lung Lin, Dr. Ming-Yang Deng, Dr. Po-Cheng Lai, Chia-Lun Lee, and Sung-Chun Chen from National Cheng Kung University for their patient and detailed discussions on display driving circuits. More importantly, the internship at Meta is a milestone in my career journey. During my internship, Dr. Yun Wang, Dr. Fenglin Peng, Dr. Anita Lu, and Dr. Yun-Han Lee gave me many valuable suggestions and inspired me to solve tough problems and exert

greater impact on future products. Also, such a valuable internship helps me revisit my previous research, stimulate more ideas, and establish a precious connection with industry. With this internship, I can organize the dissertation in a more comprehensive and consistent perspective.

Lastly, I want to thank my parents for their sincere love and care. They always support me with spiritual encouragement and comfort. Without their long-lasting care, I wouldn't have made great progress in my research. Although we are in a far distance, they continuously conveyed their care for my life and study via video calls and made me feel connected with them in my deep heart. Their love always drives me to make more contributions to human knowledge and technologies.

# TABLE OF CONTENTS

LIST OF FIGURES .....	x
LIST OF TABLES .....	xv
CHAPTER 1: INTRODUCTION .....	1
1.1 Light engines for VR .....	1
1.2 Light engines for AR .....	5
CHAPTER 2: MINI-LED BACKLIT LCDs .....	8
2.1 Background .....	8
2.2 Display metrics .....	9
2.3 Halo effect.....	14
2.4 Summary .....	18
CHAPTER 3: FIELD SEQUENTIAL COLOR LCDs FOR VR DEVICES.....	19
3.1 Background.....	19
3.2 Experiments .....	21
3.3 Simulation results.....	26
3.4 Discussions .....	35
3.5 Summary .....	36
CHAPTER 4: TANDEM WHITE MICRO-OLEDs FOR VR DEVICES .....	37
4.1 Background.....	37

4.2 Tandem white micro-OLED .....	41
4.3 Pancake optical system .....	44
4.4 Analysis and optimization.....	45
4.5 Summary .....	52
CHAPTER 5: SMALL PIXEL-SIZE LCoS FOR AR DEVICES .....	53
5.1 Background.....	53
5.2 Small pixel-size LCoS .....	53
5.3 Experimental measurements .....	60
5.4 Summary .....	64
CHAPTER 6: CONCLUSIONS .....	65
APPENDIX: STUDENT PUBLICATIONS.....	68
REFERENCES .....	74

## LIST OF FIGURES

Figure 1-1 (a) Schematic of VR and video pass-through MR. (b) FoV of human vision; (c) Schematic for calculating FoV related to eye relief and interpupil distance. ....	3
Figure 2-1 The schematic of mini-LED backlit LCDs. ....	8
Figure 2-2 Luminance dependence on the APL. ....	10
Figure 2-3 (a) Gamma curves for the mLCD and the OLED display and (b) gamma curves at low gray levels. ....	11
Figure 2-4 (a) Measurement procedure and setting for the color gamut volume and (b) measured color gamut volumes of the mLCD and the OLED display.....	13
Figure 2-5 Measured (a) white spectra and (b) color shifts of the mLCD and the OLED panels. 14	
Figure 2-6 Measurement procedure for the halo effect. ....	15
Figure 2-7 (a) Luminance profiles on the CMOS sensor for the mLCDs driven in the HDR1000 and HDR600 modes and the OLED display. (b) Real luminance profiles on the display screen for the mLCDs driven in the HDR1000 and HDR600 modes.....	16
Figure 3-1 Schematics of (a) the color filter-based AMLCD (b) the FSC AMLCD, and (c) the CBU. ....	20
Figure 3-2 Temperature-dependent birefringence at $\lambda = 633$ nm and $f = 1$ kHz (the frequency of driving voltage applied on the LC cell). Dots are measured data and the solid line is a fitting curve with Equation 3-2.....	23
Figure 3-3 Temperature-dependent visco-elastic constant. Squares are measured data and the solid line is fitting curve with Equation 3-3.....	24

Figure 3-4 Temperature-dependent figure of merit. Squares are measured data and the solid line is fitting curve with the definition of FoM.....	25
Figure 3-5 Wavelength-dependent birefringence at 22 °C. Triangles are measured data and the solid line is fitting curve with Equation 3-4.....	26
Figure 3-6 Simulated temperature dependent average GTG response time at different electrode widths and gaps.....	27
Figure 3-7 (a) Schematic of simultaneous emission (b) Schematic of progressive emission (c) Simulated CBUs corresponding to different subframe (refresh) rates.....	30
Figure 3-8 The simulated three-field Stencil algorithm including the simulated backlight layers, liquid crystal layers and front screen images.....	32
Figure 3-9 Simulated isocontrast contour for single-domain FFS mode using TechWiz software. The operating temperature is 50 °C.....	33
Figure 3-10 The spectra used in (a) FSC LCD with RGB LEDs, and (b) a blue LED, green QDs, and red QDs in the backlight module of the LCD with the QD enhancement film.....	33
Figure 3-11 Simulated color shift versus viewing angles for RGB wavelengths at horizontal (dashed lines) and vertical direction (solid line), respectively, for (a) FSC LCD with RGB LEDs, and (b) color filter based LCD with the QD enhancement film. ....	35
Figure 4-1 Various device architectures of WOLEDs. (a) 1-stack 3-color WOLED architecture, in which white light is generated by the combination of three EMLs. (b) 2-stack 2-color tandem WOLED architecture, in which white light is generated by the combination of two EMLs that are connected by a CGL. (c) 2-stack 3-color tandem WOLED architecture, in which white light is generated by the combination of three EMLs that are connected by a CGL. (d) 3-stack 3-color	

tandem WOLED architecture, in which white light is generated by the combination of four EMLs that are connected by two CGLs. (e) 2-stack 2-white tandem WOLED architecture, in which two white EMLs are connected by a CGL. ....	40
Figure 4-2 The schematic of tandem WOLED microdisplay with a patterned ITO or HIL layer below the common EMLs. ....	42
Figure 4-3 The schematic of a pancake VR system consisting of a circular polarizer, a half mirror, and a reflective circular polarizer. ....	45
Figure 4-4 The collection efficiency depending on the emission angle and the location of the point source. ....	45
Figure 4-5 The spectra of the green subpixel at different angles: 0 deg, 10 deg, and 20 deg. The emission spectra of blue and yellow-green emitters are also shown. ....	47
Figure 4-6 The CIE 1931 coordinates of the green subpixel as a function of $d_2$ at $d_4 = 10$ nm and $d_4 = 25$ nm, respectively. ....	48
Figure 4-7 Simulated color shift of the green subpixel corresponding to different source positions and HIL thicknesses ( $d_2$ ). ....	49
Figure 4-8 (a) Simulated color gamut corresponding to B/YG WOLED and B/G/R WOLED with different $d_4$ and $d_5$ . ....	51
Figure 4-9. Optimization results of WOLED microdisplays: (a) B/YG (b) high-order B/YG (c) B/G/R, and (d) high-order B/G/R. Cyan points represent optimal solutions corresponding to each case. ....	51

Figure 5-1 (a) The normalized reflectance as a function of the position at (a) different anchoring energies, and (b) different incident polarization states (linearly polarized and circularly polarized light).....	56
Figure 5-2 The normalized reflectance as a function of the position at three $\beta$ angles: $0^\circ$ , $10^\circ$ , and $20^\circ$ . .....	57
Figure 5-3 (a) The director distribution in MTN LCoS with 1.5- $\mu\text{m}$ pixel size (the pixel gap is 0.2 $\mu\text{m}$ ) (b) the depth-dependent tilt and azimuthal angles of LC directors located at three different horizontal ( $x$ -axis) positions: 1.5 $\mu\text{m}$ , 2.5 $\mu\text{m}$ , and 3.7 $\mu\text{m}$ . .....	58
Figure 5-4 Position-dependent reflectance corresponding to shielding walls with three different heights. The pixel pitch of amplitude LCoS is 3 $\mu\text{m}$ . .....	59
Figure 5-5 The position-dependent normalized reflectance with linearly polarized and circularly polarized light corresponding to (a) without shielding walls, and (b) with shielding walls. The pixel pitch is 3 $\mu\text{m}$ . .....	59
Figure 5-6 (a) Schematic of the experimental setup for measuring the FFE (b) microscopy pixel structure of the MTN LCoS panel. ....	60
Figure 5-7 (a) A microscopical image with a 40x objective lens provided by Himax (b) the frequency-dependent MTF [65] with a marked dot representing the data extracted from (a).....	61
Figure 5-8 The position-dependent reflectance using (a) white light, and (b) green light. ....	62
Figure 5-9 Comparison of the simulated FFE between two LCoS panels filled with JNC-5134 and Merck LC mixture, respectively. ....	63
Figure 5-10. Comparison of the measured FFE using a (a) 10x objective lens, and (b) 20x objective lens. ....	63

Figure 5-11. Comparison of the simulated FFE corresponding to 0.7- $\mu\text{m}$  and 1- $\mu\text{m}$  cell gaps. .. 64

## LIST OF TABLES

Table 3-1 Simulated response time of FFS mode between different gray levels without overdrive and undershoot. The operating temperature is 50 °C. ....	28
--	----

# CHAPTER 1: INTRODUCTION

Direct-view displays have played a pivotal role in our daily life, ranging from watches, smartphones, notebooks, monitors, to large screen televisions. Recently, virtual reality (VR) and augmented reality (AR) displays have gained significant momentum. Compared to direct-view displays, VR/AR devices consist of both display light engines and imaging optics (or optical combiner) to project a magnified virtual image to the user and show an advantage in generating a fatigue-free three-dimensional image. More specifically, VR devices use an imaging optics to provide immersive experience with a wide field of view (FoV); AR devices use an optical combiner to provide see-through experience with image contents overlaid with ambient environment. Therefore, the device performance, such as optical efficiency and image quality are jointly determined by the light engines and imaging optics (or optical combiner). Although a great deal of progress has been made, there is still a huge gap between current commercial products and stylish sunglasses-like VR/AR devices [1] that require a wide FoV and color gamut, sharp image, compact formfactor, and low power consumption. Therefore, there are plenty of opportunities for improvement and innovation. This dissertation is devoted to developing next-generation VR/AR light engines toward high resolution density, high optical efficiency, wide color gamut, and small form factor.

## 1.1 Light engines for VR

With the emergence of video pass-through technologies, virtual reality (VR) has gradually bridged the gap with the optical see-through AR. More specifically, full-color and high-resolution video pass-through enables a seamless transition from a fully immersive VR to a

mixed reality (MR), which allows the user to interact with the real world. For this reason, the recently launched Meta Quest 3 and Apple Vision Pro are expected to unleash the full potential of VR/MR. [Figure 1-1\(a\)](#) depicts a basic VR/MR system: a refractive lens is placed between the display panel (usually  $\sim 2$  inch) and the user's eye to magnify the image and achieve a wide FoV; several cameras capture the ambient world for video pass-through. Considering social acceptance, reverse video pass-through with an external display is an essential element to allow others to see the user's eyes. Current VR/MR headsets adopt two types of display light engines: organic light-emitting diode on silicon (OLEDoS, also called Micro-OLED) used in Apple Vision Pro, and active-matrix liquid crystal display (AMLCD) on glass used in Meta Quest 3, Pico 4 Pro, and HTC Vive Pro 2, etc. In the following, we will briefly elucidate pivotal performance metrics, including FoV, resolution density, aperture ratio and motion blur, and analyze the current challenges for light engines.

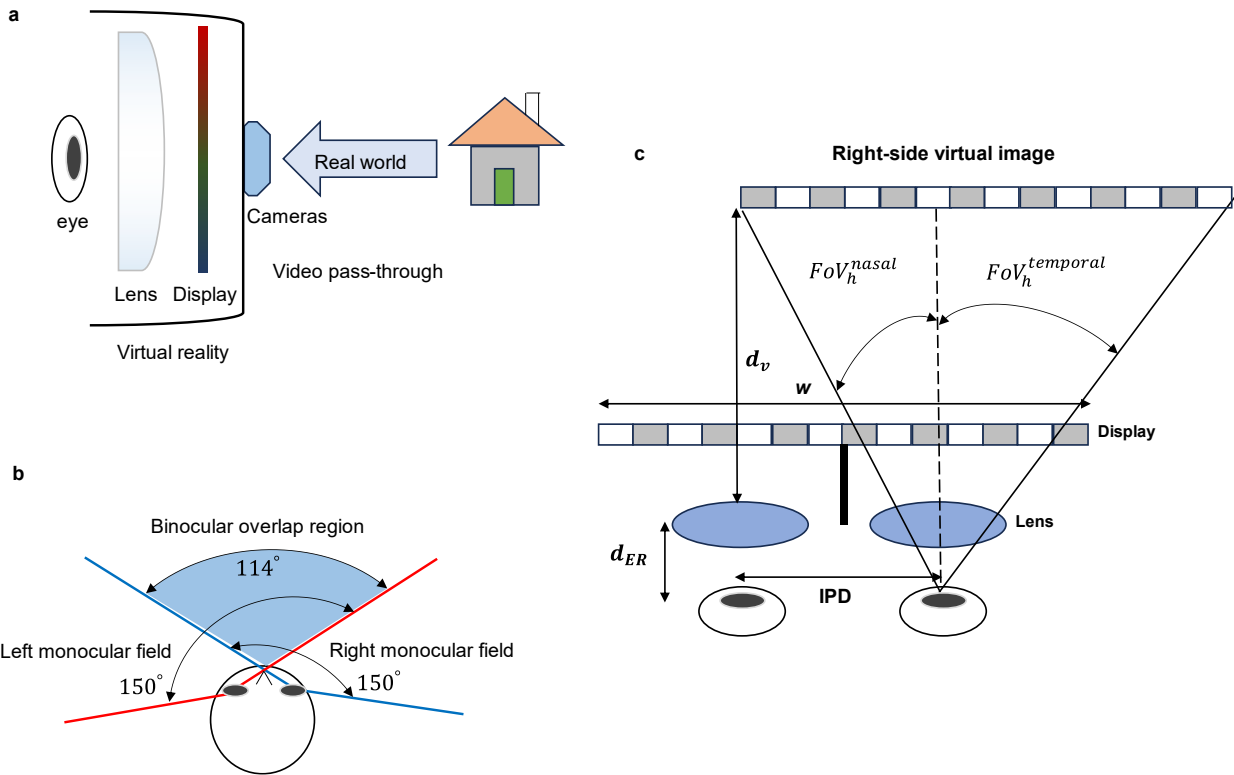


**Figure 1-1 (a) Schematic of VR and video pass-through MR. (b) FoV of human vision; (c) Schematic for calculating FoV related to eye relief and interpupillary distance.**

The first important metric is FoV, which is defined as the angular extent of the image visible to the eyes. The definition of horizontal binocular FoV can be unclear because it can refer to either binocular overlap (vision) or total monocular FoV of both eyes. For this reason, we will avoid using binocular FoV. For simplicity, we use the horizontal FoV to refer to total monocular FoV of both eyes, which VR headsets typically quote. After clarifying definitions, we can list the FoV values of the human visual system (HVS): the horizontal FoV is  $\sim 200^\circ$ , the binocular overlap FoV is  $\sim 114^\circ$ , the single-eye horizontal FoV is  $\sim 150^\circ$ , as schematized in [Figure 1-1\(b\)](#). Compared to the HVS, commercial VR headsets such as Meta Quest Pro just support a horizontal FoV of  $\sim 106^\circ$  and a single-eye horizontal FoV of  $\sim 90^\circ$ . In a VR system, the single-eye FoV can be derived below:

$$\text{FoV} \approx 2 \times \tan^{-1}\left(\frac{D/2}{f}\right), \quad (1-1)$$

where  $D$  is the panel size,  $f$  is the effective focal length of the combined viewing lenses. Equation 1-1 poses challenges to achieving a large FoV with a small microdisplay panel. For example, Apple Vision Pro adopts two 1.3-inch micro-OLED panels (one for each eye). To achieve a single-eye horizontal FoV of  $90^\circ$ , we need  $f/\# = 0.5$  (or numerical aperture NA = 0.7) under the assumption that the aperture size of optical lenses is the same as the display panel. Such a small  $f/\#$  dictates a sophisticated design of viewing optics to mitigate aberrations. A more accurate calculation of FoV should consider the interpupil distance (IPD) and eye relief (ER), as shown in Figure 1-1(c). The IPD variance across the world's population is from 51 mm to 71 mm. Therefore, the distance between two magnifying lenses can be set at an average IPD of  $\sim 61$  mm. According to Figure 1-1(c),  $FoV_h^{nasal}$  and  $FoV_h^{temporal}$  can be calculated as  $\tan^{-1}\left(\frac{IPD/2}{d_v+d_{ER}}M\right)$  and  $\tan^{-1}\left(\frac{w/2-IPD/2}{d_v+d_{ER}}M\right)$ , respectively ( $M$  is the magnification). Furthermore, the single-eye horizontal FoV is the sum of  $FoV_h^{nasal}$  and  $FoV_h^{temporal}$ , the binocular overlap FoV is  $2FoV_h^{nasal}$ , and the horizontal FoV is  $2FoV_h^{temporal}$ . According to the derived formulas, a smaller IPD leads to a smaller binocular overlap and a larger difference between the horizontal FoV and single-eye horizontal FoV. On the other hand, although a larger ER allows for the insertion of correction lens, the FoV becomes smaller.

To reproduce the clear surroundings without the screen-door effect, high-resolution density is critical. To achieve 60 pixels per degree (1 arcmin visual acuity) and a single-eye horizontal FoV of  $100^\circ$ , 6K horizontal pixels should be packed in each panel. For

transmissive AMLCDs, such a high-resolution density leads to a diminishing aperture ratio (the ratio of transmissive area to the total pixel area). A low aperture ratio will cause unwanted thermal effect and higher power consumption. In contrast to transmissive AMLCDs, micro-OLED adopts silicon backplane to achieve high-resolution density and top-emitting mechanism to enlarge the aperture ratio. Besides high-resolution density and high aperture ratio, motion blur is another important metric to evaluate the capability of displaying fast-moving objects. To mitigate motion artifacts, we usually adopt a low (10-20%) persistence (also called duty ratio; the ratio of the backlight-on time to the frame time). Such a low persistence, together with the low-efficiency pancake lens, demands a high luminance light engine. For example, to deliver 150 nits to human eyes, we need a light engine with 12500 nits, assuming 10% persistence and 12% optical efficiency. Such a high luminance poses a challenge to micro-OLEDs. According to the above analyses, further developments on display light engines are urgently needed.

### 1.2 Light engines for AR

Although VR and its pass-through MR can provide a better virtual image quality and require a lower display brightness, it is still challenging to reproduce the real ambient world because of several issues: a lower dynamic range, a lower resolution, a fixed focus, and a motion to photon delay. Therefore, optical see-through AR still exhibits enormous potential to becoming a next-generation interface between digital information and physical world. Transparent displays also provide a see-through characteristic, but the diffraction is a potential issue [2]. Because of a dictated smaller form factor of see-through AR glasses, the panel size (usually  $< 0.5$  inch) is

much smaller than that for VR displays. To pack enough (e.g. 2K) pixels in such a small panel, the required resolution density is usually larger than 5000 pixels per inch. Such a high-resolution density calls for microdisplay light engines that adopt crystalline silicon backplanes. Currently, the major competing microdisplay technologies are liquid-crystal-on-silicon (LCoS) [3], digital light processing (DLP) [4], OLED-on-silicon [5], micro-LED ( $\mu$ LED) [6] including nanowire LED [7], and laser beam scanning (LBS) [8]. LCoS and DLP are light modulation displays. LCoS utilizes voltage-induced liquid crystal reorientations to modulate the polarization state of the incoming light and pixelated metallic mirrors to reflect the modulated light. Pixelated reflectance can be obtained via converting the phase retardation to amplitude modulation after passing through the analyzer. Different from LCoS, DLP relies on rotating micromirrors to steer the incident light toward two opposite directions corresponding to on and off states. OLED and  $\mu$ LED are self-emissive displays and usually exhibit smaller form factors. In contrast to panel-based microdisplays composed of a two-dimensional pixel array, each pixel of the LBS microdisplay is formed in a time-sequential manner. Detailed working principles, merits, and demerits of each microdisplay have been extensively reviewed in previous literatures [9,10]. In this dissertation, we devote to pushing the boundary of LCoS microdisplay because it shows enormous potentials for achieving high-efficiency, high-brightness, and high-resolution waveguide-based AR glasses. In the following, we will analyze the requirement for LCoS microdisplay in an AR system, which in turn guides our research endeavor.

In a waveguide-based AR system with exit pupil expansion, a small-area in-coupler enables a compact formfactor, which in turn raises the stringent requirements for light engines: a smaller panel size and a narrower angular radiation distribution [11]. A smaller panel size also reduces

the optical engine's volume including the collimating optics. To maintain the same FoV, the focal length of the collimating lens should be shortened, and the pixel pitch should be decreased to keep the same resolution for achieving 60 pixels per degree. For example, 3- $\mu\text{m}$  pixel pitch is required to achieve 60 PPD and 50° diagonal FoV if we use a commercial diffractive waveguide combiner (Dispelix DPX 50°) whose etendue is 6.2  $\text{mm}^2\text{sr}$ , and an  $f/2$  imaging optics [12]. Compound Photonics has demonstrated 3- $\mu\text{m}$  pixel-pitch LCoS panels. To support the  $\sim 0.1$ -inch LCoS panel with a  $\sim 2\text{K} \times 2\text{K}$  resolution,  $\sim 1$ - $\mu\text{m}$  pixel size needs to be developed. On the other hand, the angular distribution of LCoS is determined by the illumination light source. The angular distribution of LED sources can be narrowed by a collimating lens. A more effective solution is to adopt laser sources because of their narrower beam spread than LEDs, if the speckles can be suppressed.

## CHAPTER 2: MINI-LED BACKLIT LCDs

### 2.1 Background

High dynamic range (HDR) is a key performance metric for display devices. According to the Dolby Research standard, HDR displays should exhibit a peak brightness of more than 4000 nits, a dark state of less than 0.005 nits, and at least a 10-bit depth of gray levels. To compete with OLED displays and other emerging displays such as micro-LED displays, the mini-LED backlit LCDs (abbreviated as mLCDs) have been rapidly developed in recent years. Through two-dimensional (2D) local dimming [13–15], mLCDs can greatly improve the contrast ratio, bit depth, and power consumption. In contrast, OLED displays offer an unprecedented contrast ratio, faster response time, thin profile, and excellent flexibility, but the tradeoff between brightness and lifetime remains to be overcome [16]. [Figure 2-1](#) describes the system configuration of a mini-LED backlit LCD. The backlight system consists of blue mini-LEDs on reflective printed circuit board (PCB), diffuser sheets, a color conversion film, and two brightness enhancement films (BEFs). Diffuser sheets facilitate the homogeneousness of blue light, and a color conversion film transforms the blue light into white light.

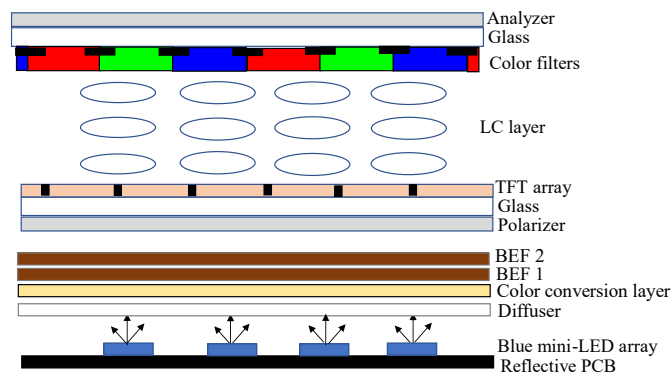


**Figure 2-1** The schematic of mini-LED backlit LCDs.

Among many kinds of direct-view displays, the competition in the notebook market is especially fierce. To answer “mLCD or OLED: who wins?”, we systematically measured and compared the display performance of Nichia’s 15.6” mLCD panel with a 15.6” commercial OLED notebook computer (Dell XPS 15 7590). We evaluated their brightness, gamma curve, color volume, color shift, and halo effect. In comparison with previous methods, our color measurement adopted the reference method recently recommended by the International Committee for Display Metrology (ICDM), and the three-dimensional (3D) display gamut envelopes were created from 602 measured surface colors. Furthermore, we used the LMK imaging photometer (TechnoTeam Vision) with a high-resolution CMOS (complementary metal-oxide semiconductor) image sensor to characterize the halo effect and reconstruct the real luminance profiles based on the non-ideal profile of the OLED display. The point spread function (PSF) of the backlight module was also measured using a novel strategy without requiring physical separation between the backlight and the liquid crystal (LC) module [17]. It is noted that since mini-LEDs can be also used in the VR devices (Chapter 3) and AR devices, the performance metrics and methodologies in this chapter are helpful for developing and evaluating the VR and AR devices.

## 2.2 Display metrics

To characterize the effect of luminance loading, the luminance of a white box with a black background was measured using the LMK when the white box size varied from a small fraction to the full screen. The white area size ratio (average picture level (APL)) ranging from 0.01% to 1% can be used to imitate the shining stars in a black sky. According to [Figure 2-2](#), the mLCD

showed a higher brightness than the OLED display when  $APL \geq 1\%$ . As the APL increased from 0.01% to 100%, the OLED brightness decreased from 562 nits to 431 nits, while the mLCD increased from 233 nits to 997 nits. When the bright area shrunk to a very small size, the zone crosstalk became more evident. For this reason, the mLCD brightness was adjusted to a relatively low value. For most of the image contents with  $APL \geq 1\%$ , the mLCD had a much better HDR performance.

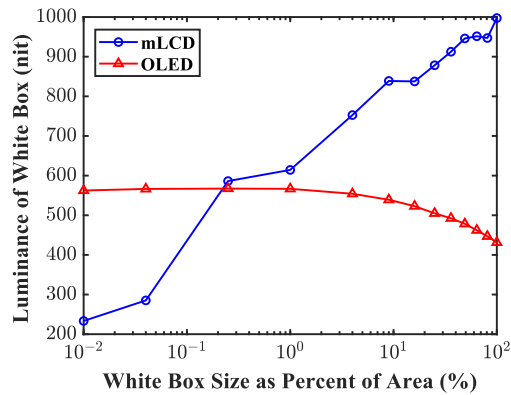


**Figure 2-2 Luminance dependence on the APL.**

The gamma curves of the mLCD and the OLED display panels were obtained by measuring the luminance at gray levels ranging from 0 to 255. In Figure 2-3(a), the dots represent the measured data, and the solid lines are the fitting curves. The fitted gamma values of the mLCD and the OLED display were 2.6 and 2.2, respectively. Figure 2-3(b) shows the luminance values and gamma curves at low gray levels. The OLED display deviated from the expected gamma 2.2 curve noticeably due to its much higher luminance values from the third to the eighth gray levels, which may arise from inaccurate current control at low gray levels.

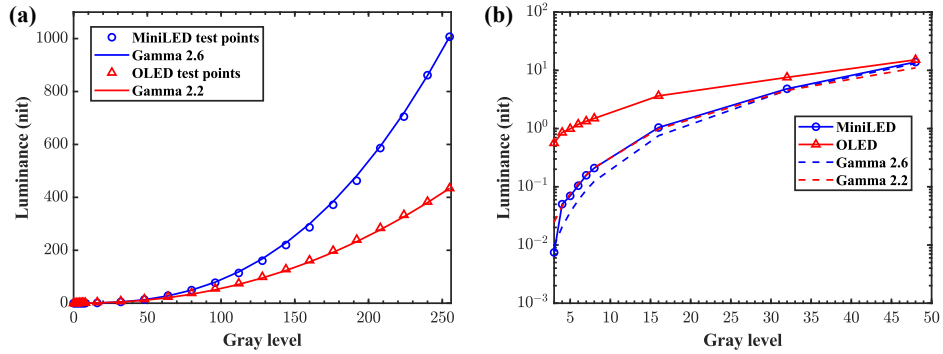


**Figure 2-3 (a) Gamma curves for the mLCD and the OLED display and (b) gamma curves at low gray levels.**

Color gamut and color shift are two important metrics to evaluate the color performance of a display panel. A good display should exhibit a wide color gamut and a weak color shift. The color gamut of a display is better represented by a 3D volume instead of a chromaticity gamut area. The gamut envelope is calculated in the human perceptual color space CIE 1976  $L^*a^*b^*$  due to its good perceptual homogeneity. Our measurement procedure follows the reference method that the ICDM recommends. In this method, the full 602-color reference sets should be used if the behavior of the display panel is not well known. The measurement procedure and setting are explicitly illustrated in Figure 2-4(a). The first step was to generate 602 color images in the Rec.2020 color space. These 602 unique colors were evenly distributed on the linear RGB (red, green, blue) signal space. Then, we measured the tristimulus values ( $X$ ,  $Y$ ,  $Z$ ) of each color using the LMK with full glass filters for color matching functions. Next, a chromatic-adaptation transform was built to adapt the measured values from the display white point to the standard illuminant D50 using the modified Bradford adaptation transform method. The last step was to calculate the CIE 1976 D50  $L^*a^*b^*$  coordinates from the converted tristimulus values as follows:

$$L^* = 116 \times f\left(\frac{Y}{Y_n}\right) - 16, \quad (2-1)$$

$$a^* = 500 \times \left[ f\left(\frac{X}{X_n}\right) - f\left(\frac{Y}{Y_n}\right) \right], \quad (2-2)$$

$$b^* = 200 \times \left[ f\left(\frac{Y}{Y_n}\right) - f\left(\frac{Z}{Z_n}\right) \right], \quad (2-3)$$

$$f(t) = \begin{cases} t^{1/3} & t > (6/29)^3 \\ \frac{1}{3} \left(\frac{29}{6}\right)^2 t + \frac{16}{116} & \text{otherwise} \end{cases} \quad (2-4)$$

where  $(X_n, Y_n, Z_n)$  is the D50 with a certain white luminance. To compare the color gamut volumes of the mLCD and the OLED display, their different brightnesses should be considered as well. For this reason, the white luminance was set to the white brightness of the mLCD to reflect that the brightness can greatly impact the color gamut volume. The color gamut volumes of the mLCD and the OLED display are shown in [Figure 2-4\(b\)](#). According to the gamut envelope, the color space of the mLCD and the OLED display had a CIELAB gamut volume of 1191300  $\Delta E^3$  and 650680  $\Delta E^3$ , respectively. In terms of the reference Rec.2020 color space, the percentages of coverage for the mLCD and the OLED display were 64.3% and 35.0%, respectively. The mLCD exhibited a larger color gamut volume than the OLED display due to its higher peak brightness.

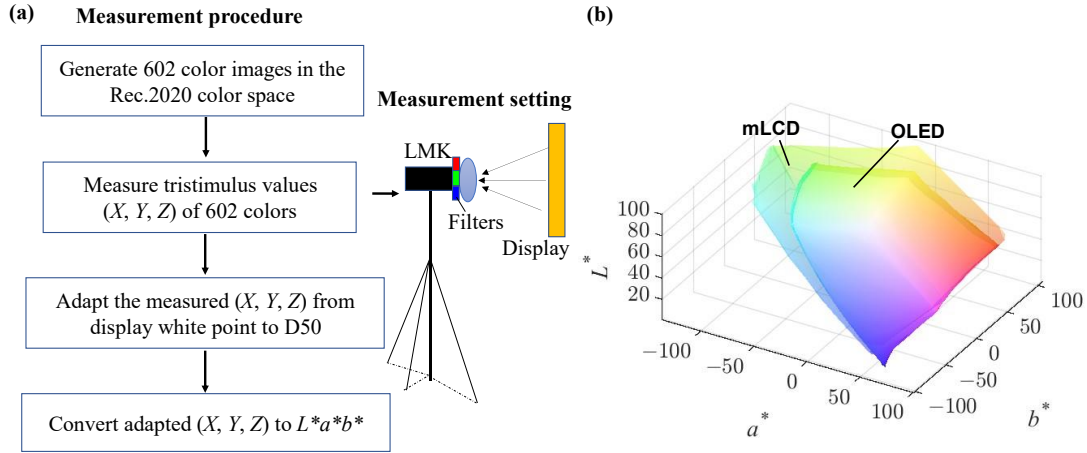


**Figure 2-4 (a) Measurement procedure and setting for the color gamut volume and (b) measured color gamut volumes of the mLCD and the OLED display.**

Color shift is another important parameter to evaluate the color uniformity of a display panel. The angular color shift can be impacted by both the variations of primary RGB colors and unmatched angular distributions of primary colors according to the color mixing principles. For an mLCD, its angular color shift arises from the angle-dependent accumulated phase retardation in the birefringent LC layer. When the incident light transverses the LC layer at different angles, the accumulated phase retardation varies, giving rise to the angle-dependent transmittance and color shift. For this reason, the color coordinates of primary colors vary with viewing angles. For an OLED display, the variations of primary colors are attributed to the cavity effect. As the viewing angle increases, the emission spectrum shifts toward a shorter wavelength because of the reduced effective cavity length. On the other hand, if the angular distributions of primary colors are not matched well, the mixed colors will vary with the viewing angle due to angle-dependent RGB ratios [18,19].

The experimental procedure to measure color shift is described as follows: we first measured the white spectrum using a high-resolution spectrometer (HR2000CG-UV-NIR); then, we rotated

the angle of the optical fiber used for collecting white light into the spectrometer and measured the white spectrum again at different viewing angles. Figure 2-5(a) shows the measured white spectra of the mLCD and the OLED display at 0° and 60° viewing angles. From Figure 2-5(a), we can see that the mLCD backlight adopted two phosphors to widen the color gamut, while the blue shift caused by the cavity effect was noticeable for the OLED panel. As Figure 2-5(b) depicts, the mLCD exhibited a weaker color shift than the OLED display. The weaker color shift of the mLCD benefited from the small color shift of the fringing field switching (FFS) mode. It should be mentioned that the color shift remains indistinguishable by human eyes if  $\Delta u'v' < 0.02$ . This means that both panels are fine in terms of color shift within the 60° viewing cone.

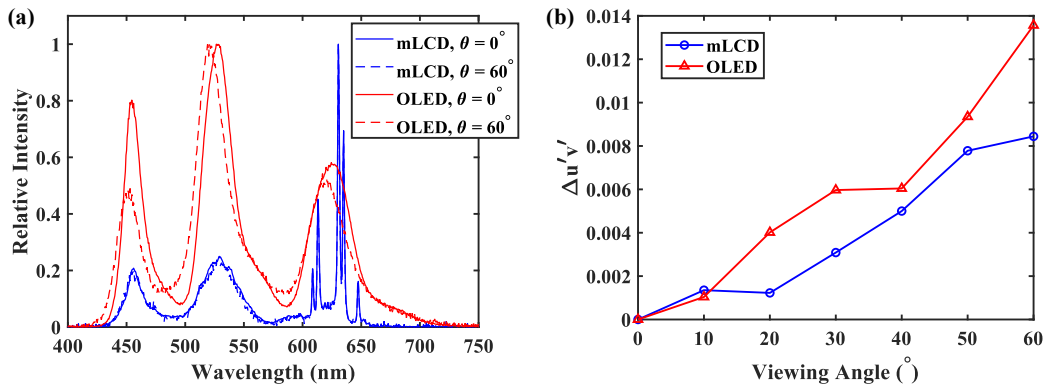


**Figure 2-5 Measured (a) white spectra and (b) color shifts of the mLCD and the OLED panels.**

### 2.3 Halo effect

The halo artifact usually appears around a bright object on a black background due to the light leakage and the zone crosstalk in an mLCD panel. The experimental procedure to quantitatively characterize the halo effect is illustrated in Figure 2-6. We first inputted a test pattern with a white cross on a black background. Then, we used the LMK to obtain a luminance

distribution image. A halo image could finally be generated by excluding the luminance pattern of the cross from the luminance distribution image, where the halo artifacts surrounding the cross were more visible. Based on the measured RMS and SD values, we could quantitatively analyze and compare the halo effect for the generated halo images. The values of the RMS and SD for the mLCD driven in the HDR1000 and HDR600 modes and the OLED display were [0.2379, 0.2339], [0.1916, 0.1893], and [0.1830, 0.1811], respectively. The halo of an OLED display is caused by the measurement instrument, such as an imaging lens. Such a halo is analogous to the eye halo [15].

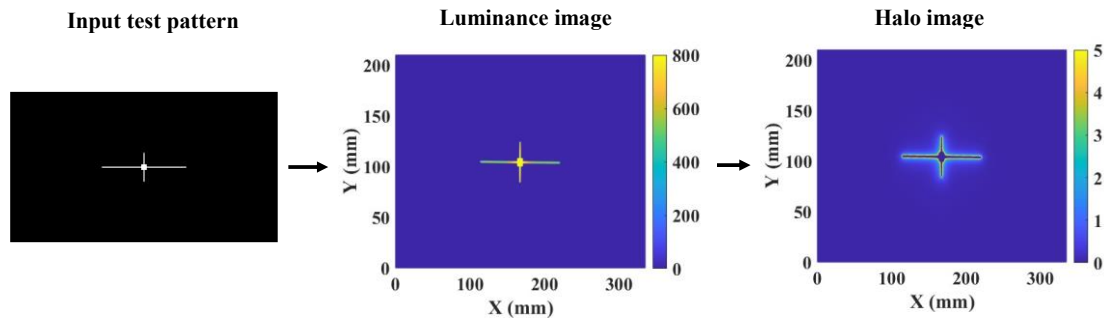


**Figure 2-6 Measurement procedure for the halo effect.**

So far, we have characterized and compared the halo effect by obtaining the images on the CMOS sensor. The cross-section luminance profiles are shown in [Figure 2-7\(a\)](#), where the luminance profile for the OLED display is non-ideal and the lines are all broadened due to a gradient drop in the 1D luminance distribution caused by the imaging instruments. To obtain the real luminance profiles for the displayed images, the non-ideal luminance profile for the OLED display can be used as a background reference and accordingly subtracted in the region outside the displayed line. In this way, an ideal luminance profile for the OLED display should be a rectangular function from zero to the maximum luminance. For the mLCD, its luminance profile

was also narrowed to a rectangular line with the same method. The difference lies that the luminance outside the line will not quickly drop to zero, depending on how many zones are lit, because the contrast ratio in those lit zones is still limited by the LC layer. Figure 2-7(b) shows the real luminance profiles for the mLCDs driven in the HDR1000 and HDR600 modes. Taking the HDR600 driving mode as an example, the maximum and minimum luminance in the lit zones were 490 nits and 0.2 nits, respectively, indicating a contrast ratio of 2450:1. This contrast ratio was quite close to that of the FFS mode, whose CR was about 2500:1, which validated our methods for obtaining the real luminance profiles from imaging instruments. Furthermore, it can be inferred that five zones were lit in this selected cross-section due to the nearly constant value of 0.2 nits, ranging approximately from  $-20$  mm to  $20$  mm. The five lit zones were possible if the selected cross-section was very close to the center portion of the cross. It should be mentioned that for the HDR1000 driving mode, a scaling luminance factor should be considered due to a significant luminance difference between the mLCD driven in the HDR1000 mode and the OLED display.

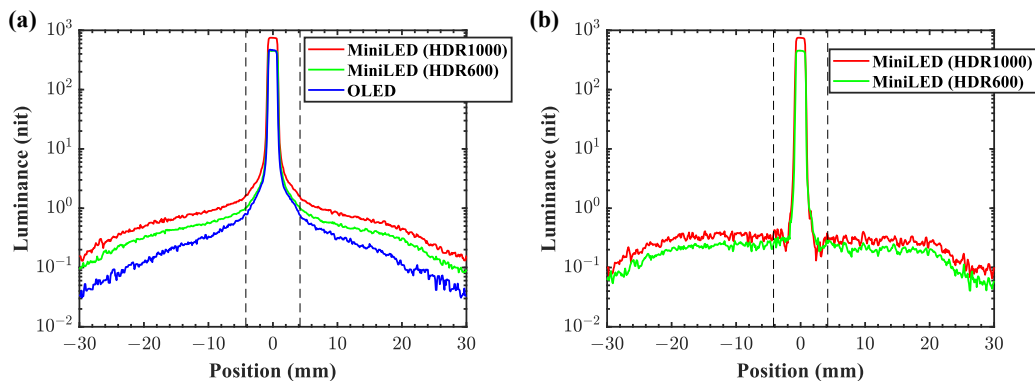


**Figure 2-7 (a) Luminance profiles on the CMOS sensor for the mLCDs driven in the HDR1000 and HDR600 modes and the OLED display. (b) Real luminance profiles on the display screen for the mLCDs driven in the HDR1000 and HDR600 modes.**

As mentioned before, the contrast ratio inside the lit zones is limited by the intrinsic CR of the LC mode. In the boundary areas between lit zones and closed zones, it is also hard to obtain a sharp transition of the luminance profile due to the zone crosstalk characterized by the point spread function. To measure the point spread function of the backlight module, we first inputted a display pattern of two thin lines to make sure that just one zone was lit in the direction perpendicular to the line. Next, we adopted a novel strategy without requiring the physical separation between the LC layer and the backlight module. This method takes advantage of a limited contrast ratio of the FFS mode and a very bright backlight. Furthermore, this method is enabled because the backlight is independent of the LC driving signal. For this reason, instead of removing the LC layer, we turned off the voltage applied on the LCs, and then the LCs at the dark state exerted a uniform modulation on the pattern of the mini-LED backlight. The luminance profile of the backlight modulated by the LCs was detectable by the LMK because its luminance value was still within the measurement range. Therefore, we used the LMK to measure the point spread function of the backlight module by obtaining the luminance distribution image, as shown in [Figure 2-8\(a\)](#). The point spread function of a zone along the y-axis at  $x = 1$  mm is shown in [Figure 2-8\(b\)](#). In Nichia's mLCD, each zone contained one mini-LED; therefore, we could equate the light profile of a single mini-LED with the point spread function of a zone. The Gaussian function can be used to approximate the light profile of a mini-LED:

$$I(x_{LED}) \propto \exp\left[-\frac{(x_{LED}-x_{LED,c})^2}{2\sigma^2}\right] \quad (2-5)$$

where  $x_{LED,c}$  is the locus of the LED source and  $\sigma$  is an expansion characteristic parameter. Good fitting was obtained with  $\sigma = 6.5$  mm. A small  $\sigma$  value helps confine light inside the zone.

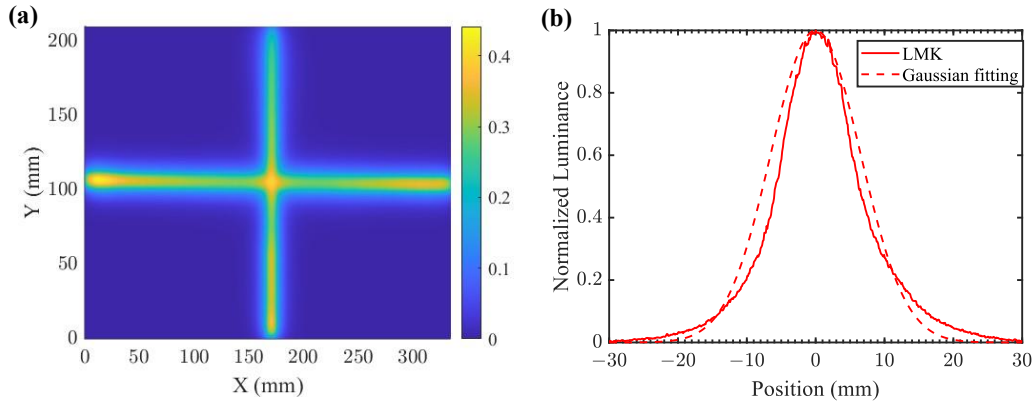


**Figure 2-8. (a) Two-dimensional luminance distribution for the backlight. (b) One-dimensional luminance profile.**

## 2.4 Summary

Using quantitative measurement data, Nichia’s 15.6-inch mLCD showed several advantages over the commercial OLED display panel in peak brightness, accurate gamma curve, color gamut volume, and ambient contrast ratio. Their color shifts remained indistinguishable by human eyes when the viewing cone was within  $60^\circ$ . The confining reflector wall helped reduce the zone crosstalk and the halo effect. The LMK with a high-resolution CMOS sensor was employed to characterize the halo effect and reconstruct the real luminance profiles. We also adopted a novel strategy to measure the point spread function of the backlight module. In the chapter 3, we will leverage such a mini-LED backlight to achieve progressive emission and enable a higher subframe rate for field sequential color LCDs.

## CHAPTER 3: FIELD SEQUENTIAL COLOR LCDs FOR VR DEVICES

### 3.1 Background

Display light engines play a vital role affecting the performance of virtual reality (VR) headsets. Recently, JDI and Innolux independently demonstrated a 2.27” 2016 pixels per inch (PPI) active-matrix liquid crystal display (AMLCD) with subpixel rendering for VR displays. Such a light engine offers 32 pixels per degree (PPD) and 100° single-eye horizontal field of view (FoV), but its aperture ratio is lower than 10%, implying to a relatively large power consumption. To achieve 60 PPD and 100° single-eye horizontal FoV with a color filter based AMLCD ([Figure 3-1\(a\)](#)), the required PPI should be 3780 given the same 2.27” panel size [20]. Under such a high-resolution density, the extrapolated aperture ratio would be < 1% [21], which implies to a high-power consumption. To enlarge the aperture ratio of high-PPI AMLCDs, field sequential color (FSC) is a viable approach. Instead of spatial color mixing, FSC AMLCDs leverage temporal color mixing of several flashing subframe images, as shown in [Figure 3-1\(b\)](#). By eliminating the spatial color filters, both resolution density and optical efficiency are tripled [22]. Thus, the required resolution density can be reduced from 3780 PPI to 1260 PPI in the horizontal direction.

Although FSC AMLCDs have tremendous benefits, the color breakup (CBU) hinders its widespread application. [Figure 3-1\(c\)](#) explains the origin of the CBU: when a saccadic eye movement or smooth pursuit of a moving object induces a relative speed between the viewer’s eye and the image, the sequentially flashing subframe images cannot be perfectly overlapped on the retina, leading to the CBU. When the subframe images move toward the right direction relative to the human eyes, the red fringe and blue fringe will occur in the most left and most

right of an image (Figure 3-1(c)). The green subframe may mix with the preceding red and succeeding blue subframe to generate intermediate yellow and cyan colors in the left and right side, respectively (Figure 3-1(c)). To quantitatively evaluate the CBU, we first simulate CBU images by shifting each subframe for a certain number of pixels relative to a preceding subframe. Then we calculate the difference between CBU images with original images using an average CIEDE2000 color difference. The shift value  $d$  in pixels can be calculated by:

$$d = \frac{w}{FoV} \cdot \frac{v}{R} \cdot DR \quad (3-1)$$

where  $w$  is the horizontal resolution in pixels,  $v$  is the moving speed in degrees per second,  $R$  is the subframe (refresh) rate in Hertz, and  $DR$  is the duty ratio, which is the ratio of the backlight-on time to the frame time. According to Equation 3-1, a straightforward method of suppressing the CBU is to pursue a higher subframe rate  $R$  and thereby reducing the shift value  $d$  among the subframes.

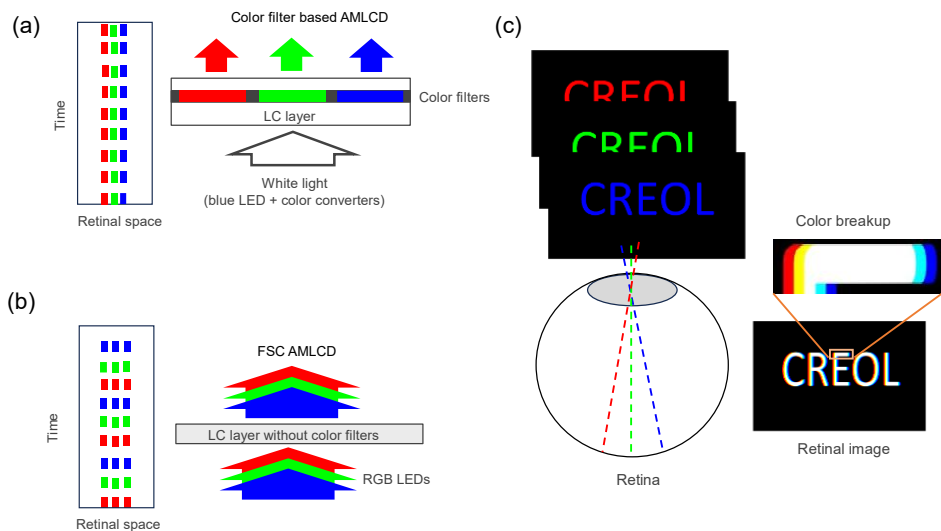


**Figure 3-1 Schematics of (a) the color filter-based AMLCD (b) the FSC AMLCD, and (c) the CBU.**

Fast LC response time is critical for achieving a high subframe rate. One approach is to use ferroelectric liquid crystals (FLCs) because of its microsecond response time [23,24]. However, the driving circuits for realizing gray levels are complicated. For example, a 3T1C (three transistors and one capacitor) pixel circuit and DC compensation driving frame are adopted to generate 8-bit gray levels for electrically suppressed helix FLC [24]. The increased space for multiple transistors would undoubtedly lower the resolution density, while the DC compensation would reduce the frame rate; both are undesirable for VR displays. In contrast, nematic LCD is easy to drive just using 1T1C (one transistor and one capacitor), but its response time is usually slower. Polymer-stabilized blue-phase LCs [25] can exhibit sub-millisecond response time, but the operation voltage is still high and slow capacitor charging requires the pre-charging method. To achieve fast response time while keeping a low driving voltage, a high birefringence and low viscosity nematic LC mixture needs to be developed and evaluated. High birefringence enables a thin cell gap to be used [26], which helps decrease response time and crosstalk. In a pancake-lens based VR headset, the housing temperature can easily reach 50-60 °C because of the thermal effect from the light engine and imaging optics. On the positive side, such an elevated temperature helps to lower the LC viscosity dramatically.

### 3.2 Experiments

As the technology keeps evolving, several compact LCD light engines for VR headsets have been developed. For example, TCL presented a 1.77" ultracompact LCD at Display Week 2022. Such a small panel size enables a cell gap as thin as 2  $\mu\text{m}$  to be fabricated. In contrast, a typical cell gap for the small LCoS panels is around 1  $\mu\text{m}$ . Such a thin cell gap helps to decrease

response time and crosstalk, but a high birefringence LC is needed. To prove concept, we use a new LC mixture formulated by JNC, designated as ZHX-5134, for thin cell FFS LCD. The optimized LC mixture features a high clearing temperature, high birefringence, large dielectric anisotropy, and relatively low viscosity. High clearing point helps the LCD withstand a high operating temperature, which is urgently needed in next-generation high-dynamic-range VR headsets where an ultrahigh brightness is needed.

Pancake optical system is dominating the VR headsets because of its compactness [27]; however, its optical efficiency is reduced by 4x because of the employed half mirror. A lower optical efficiency requires a brighter light engine to achieve the same brightness. Thus, the working temperature of the light engine can easily reach 50-60 °C by the thermal effect. The LCD light engine using an LC mixture with high clearing point is desirable. Therefore, it is necessary to systematically measure the temperature-dependent birefringence, visco-elastic constant, and figure of merit (FoM), which greatly impact the transmittance and response time of the AMLCD light engines.

To measure the temperature-dependent birefringence, we filled the LC mixture into a commercial homogeneous cell with the cell gap of 5.37  $\mu\text{m}$ . Next, we used a Linkam heating stage (Linkam TMS94) to control the operating temperature. The test cell was sandwiched between two crossed polarizers. The probing beam was a He-Ne laser ( $\lambda = 633 \text{ nm}$ ). The temperature-dependent birefringence can be calculated from the measured voltage-dependent transmittance at each temperature. Results are shown as the black dots in [Figure 9](#). The solid line represents Haller's semi-empirical equation [28]:

$$\Delta n(T) = \Delta n_0 S = \Delta n_0 (1 - T / T_c)^\beta, \quad (3-2)$$

where  $T_c$  is the clearing temperature,  $\beta$  is the material constant,  $S$  is the order parameter, and  $\Delta n_0$  is the extrapolated birefringence at  $T = 0$ . Using Equation 3-2 to fit the experimental data, we obtained  $\Delta n_0 = 0.277$  and  $\beta = 0.237$ . As Figure 3-2 depicts, the experimental data agree well with the fitting curve. As the temperature ( $T$ ) approaches  $T_c$  ( $\sim 96$  °C),  $\Delta n$  decreases rapidly. High clearing temperature plays an important role to keep a high birefringence for the AMLCD to operate at an elevated temperature (50-60 °C) while the viscosity is reduced substantially.

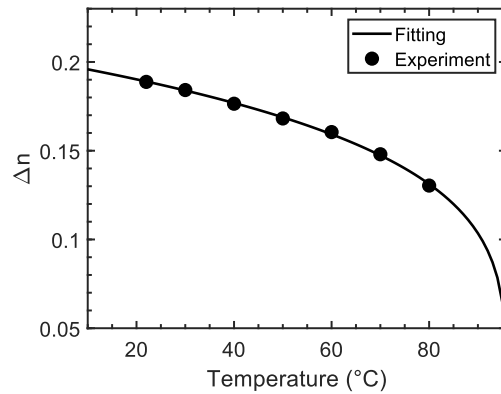


**Figure 3-2 Temperature-dependent birefringence at  $\lambda = 633$  nm and  $f = 1$  kHz (the frequency of driving voltage applied on the LC cell). Dots are measured data and the solid line is a fitting curve with Equation 3-2.**

Temperature-dependent visco-elastic constant directly impact the LC response time. The visco-elastic constant ( $\gamma/K_{11}$ ) can be extracted from the measured time-dependent relaxation process of a homogenous cell. As the temperature increases,  $\gamma/K_{11}$  decreases rapidly and then saturates, as described below [29]:

$$\frac{\gamma_1}{K_{11}} = A \frac{\exp(E_a / k_B T)}{(1 - T / T_c)^\beta}, \quad (3-3)$$

where  $A$  is the proportionality constant,  $E_a$  is the activation energy, and  $k_B$  is the Boltzmann constant. Using Equation 3-3 to fit the experimental data indicated by black squares in Figure 3-3, we found  $A = 1.54 \times 10^{-5} \text{ ms}/\mu\text{m}^2$  and  $E_a = 334 \text{ meV}$ .

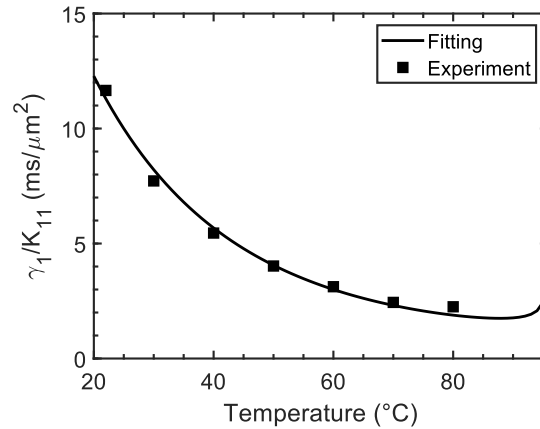


**Figure 3-3 Temperature-dependent visco-elastic constant. Squares are measured data and the solid line is fitting curve with Equation 3-3.**

As shown in Figure 3-2 and Figure 3-3, both birefringence and visco-elastic constant vary with temperatures but at different rates. To find an optimal operating temperature, a figure of merit is defined as  $\text{FoM} = \Delta n^2 / (\gamma / K_{11})$  to take both factors into account [30]. According to Figure 3-4, the optimal operating temperature occurs at  $\sim 70 \text{ }^\circ\text{C}$ , and the FoM at  $T = 50 \text{ }^\circ\text{C}$  is 2.3x higher than that at  $T = 22 \text{ }^\circ\text{C}$ . A more comprehensive FoM also includes the effect of dielectric anisotropy  $\Delta\epsilon$ . A larger  $\Delta\epsilon$  enables a lower threshold voltage and operating voltage, but the viscosity may inevitably increase. For this LC mixture, there is a good balance between viscosity and dielectric anisotropy ( $\Delta\epsilon = 6.9$  at  $T = 25 \text{ }^\circ\text{C}$  and  $f = 1 \text{ kHz}$ ). As the temperature increases, the dielectric anisotropy decreases. At  $T = 50 \text{ }^\circ\text{C}$  and  $f = 1 \text{ kHz}$ ,  $\Delta\epsilon$  is decreased from 6.9 to 6.1.

Compared to previously reported low viscosity materials used in FFS cells [31,32], this LC mixture can exhibit a lower operating voltage.

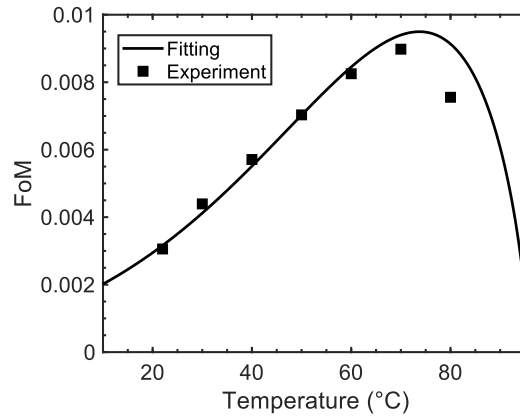


**Figure 3-4 Temperature-dependent figure of merit. Squares are measured data and the solid line is fitting curve with the definition of FoM.**

Birefringence dispersion is also an important factor for full-color VR displays. To measure birefringence dispersion, a tunable Argon ion laser (457 nm, 488 nm, and 514 nm) and a He-Ne laser (633 nm) were employed as probing beams. Results are shown as black triangles in Figure 3-5. To calculate the birefringence at other wavelengths (especially at 450 nm, 550 nm, and 650 nm), we refer to single-band birefringence dispersion equation [33]:

$$\Delta n = G \frac{\lambda^2 \lambda^{*2}}{\lambda^2 - \lambda^{*2}}, \quad (3-4)$$

where  $\lambda^*$  is the mean resonance wavelength and  $G$  is the proportional constant. Using Equation 3-4 to fit the experimental data, we found  $\lambda^* = 0.252 \mu\text{m}$ , and  $G = 2.48 \mu\text{m}^{-2}$ . According to the fitting curve (black solid line) in Figure 4, the birefringence at  $\lambda = [450 \text{ nm}, 550 \text{ nm}, 650 \text{ nm}]$  and  $T = 22 \text{ }^\circ\text{C}$  is  $[0.231, 0.200, 0.186]$ , respectively.

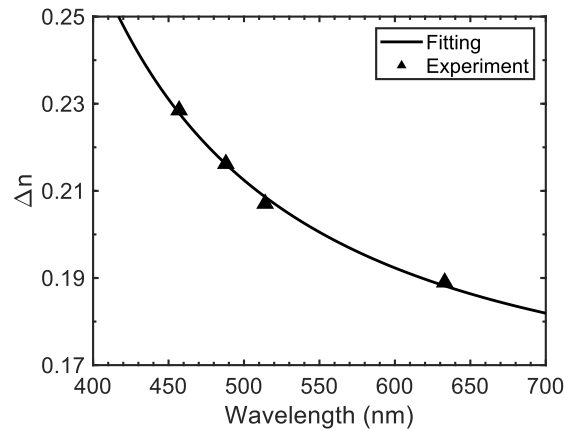


**Figure 3-5 Wavelength-dependent birefringence at 22 °C. Triangles are measured data and the solid line is fitting curve with Equation 3-4.**

### 3.3 Simulation results

For VR displays, single domain LCD may be sufficient because of the narrow collection cone ( $\sim 20^\circ$  to form decent eyebox) limited by human eyes. Therefore, we chose a single domain FFS LCD because of its wide viewing angle and weak color shift. On the other hand, FSC LCDs rely on the human vision system to integrate three successive (RGB) images into a color image. For this reason, the LC response time should be fast enough, depending on the required (sub)frame rate. Variable frame rates are employed for different tasks. For example, the Meta Quest Pro features a 90 Hz maximum refresh rate (72 Hz mode available) targeted for office tasks. Games and videos may require a higher frame rate, e.g., 120 Hz. Therefore, the virtual wall [34,35] is employed to further decrease the response time and achieve a fast color subframe. To determine the appropriate electrode width and gap, we employed TechWiz LCD 3D (Sanayi, Korea) to simulate the voltage-dependent transmittance and average gray-to-gray (GTG) response time, corresponding to a series of different electrode widths and gaps. The simulation conditions include a  $2^\circ$  pretilt angle and  $0^\circ$  rubbing angle. The cell gap is  $2 \mu\text{m}$ , which helps

decrease response time and crosstalk while keeping a good manufacturing yield. The pixel pitch  $L = 6 \mu\text{m}$ , which has been recently realized [36]. Figure 3-6 shows that finer electrode widths ( $w$ ) or gaps ( $g$ ) help decrease the response time. For example,  $w = 1.5 \mu\text{m}$  and  $g = 1.5 \mu\text{m}$  can achieve an average GTG response time of  $< 3.7 \text{ ms}$  (top horizontal dashed lines) at  $T > 22 \text{ }^\circ\text{C}$  and  $2.7 \text{ ms}$  (bottom horizontal dashed lines) at  $T > 30 \text{ }^\circ\text{C}$ . As  $T$  increases, the average GTG response time decreases rapidly because of the decreased viscosity.

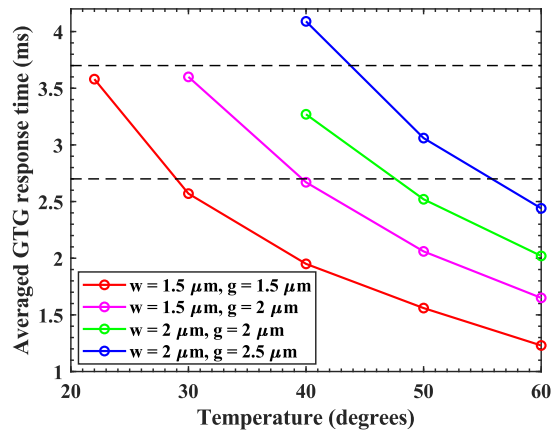


**Figure 3-6 Simulated temperature dependent average GTG response time at different electrode widths and gaps.**

Table 3-1 lists the rise time and decay time corresponding to different gray levels at  $50 \text{ }^\circ\text{C}$ . To calculate the GTG response time, the voltage-dependent transmittance curve is uniformly divided into 256 gray levels. The response time between 0, 64, 128, 192, and 255 gray levels is then obtained by calculating the transition time between 10% and 90% transmittance change. The fastest GTG response time is  $0.62 \text{ ms}$  and the average GTG response time is  $1.5 \text{ ms}$ , which leaves more time for the gate lines to be scanned and for the backlight to be turned on. Overdrive and undershoot can be further employed to achieve sub-millisecond response time of LCs, thus enabling a fast response time for lower temperature operation, but the driving circuitries are

more complicated. Despite a fine electrode pitch, a relatively low threshold voltage of  $\sim 1.6$  V<sub>rms</sub> is obtained, arising from a decent dielectric anisotropy. The normalized transmittance for red, green, and blue (RGB) wavelengths almost saturates at 6 V<sub>rms</sub>, where the transmittance of 52% is achieved at  $\lambda = 450$  nm.

**Table 3-1 Simulated response time of FFS mode between different gray levels without overdrive and undershoot. The operating temperature is 50 °C.**

		Rise time (ms)				
Gray level		0	64	128	192	255
Decay time (ms)	0	\	2.17	1.97	1.77	1.74
	64	0.62	\	1.75	1.64	1.84
	128	0.65	1.65	\	1.60	2.07
	192	0.69	1.58	1.61	\	2.50
	255	0.75	1.51	1.57	1.60	\

In previous parts, a fast LC response time of average 1.5 ms using a high birefringence material and zero-degree rubbing angle has been achieved. The maximum achievable subframe rate also depends on the driving methods. [Figures 3-7\(a\) & 3-7\(b\)](#) show the timing diagram of AMLCDs with simultaneous emission and progressive emission, respectively. In the simultaneous emission, the backlight is turned on following the scanning process and the LC reorientation, as indicated by the green box in [Figure 3-7\(a\)](#). A short backlight-on window helps reduce the motion blur via enabling a low duty ratio, but an instant high current is required to generate the targeted brightness. A larger driving current of the power source may reduce the LED backlight efficiency and worsen the current-resistance effect (I-R drop) on the power source line. Besides, the LC transition and backlight-on window account for a certain portion of

frame time and thus limits the subframe rate. For the progressive emission, a mini-LED backlight is required to turn on backlight zones sequentially after the scanning process and the LC reorientation. Because the backlight of each block in [Figure 3-7\(b\)](#) is independent, the backlight of the first few blocks can be turned on while the LCs of the last few blocks are still under reorientation. In this way, the subframe rate of the display can be higher. Such a progressive emission, together with fast scan time (e.g. 1.7 ms), allows for a ~ 600 Hz subframe rate. It is noted that for progressive emission, the sum between a fast LC response time (1.5 ms) and backlight-on time (0.17 ms corresponding to 10% persistence) should be less than a subframe time to preserve image fidelity. As a comparison, simultaneous emission just enables a ~ 300 Hz subframe rate because of the inclusion of LC response time and backlight-on time. Such a fast scan time can be achieved via writing data for multiple ( $n$ ) gate lines in different blocks synchronously. In this manner, the scan time can be greatly reduced by  $n$  times. Inevitably, the number of data lines is increased by  $n$  times. Fortunately, the data lines can be reduced by 3x because of the color sequential display. Through a high subframe rate, the CBU can be mitigated because of reduced spatial shift among the subframes, but the dynamic electrical power consumption may increase.

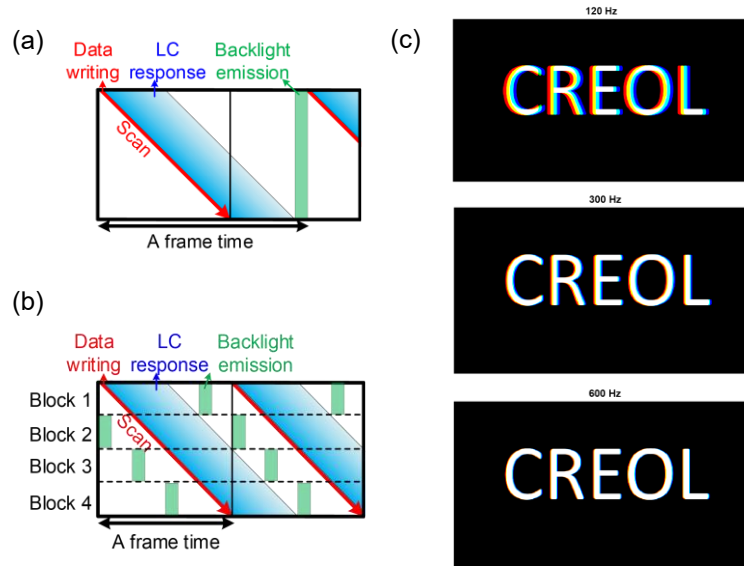


**Figure 3-7 (a) Schematic of simultaneous emission. (b) Schematic of progressive emission. (c) Simulated CBUs corresponding to different subframe (refresh) rates.**

To evaluate how our proposed methods mitigate the CBU, we first simulate CBU images via shifting the subframes accordingly. To determine the shift value, we need to dictate a series of parameters: the horizontal resolution is 4K, the single-eye FoV is  $90^\circ$ , the moving speed is 200 degrees/s (usually ranging from 100 to 300 degrees/s), and the duty ratio is 20%. The remaining parameter is the subframe (refresh) rate. The normal AMLCD has a refresh rate of 120 Hz. With our fast-response LC material and structure, the refresh rate can be increased to 300 Hz or 600 Hz, corresponding to simultaneous emission or progressive emission. Based on the above parameters, when the refresh rates are 120 Hz, 300 Hz, and 600 Hz, respectively, the calculated shift values are 15 pixels, 6 pixels, and 3 pixels, respectively. Figure 3-7(c) show simulated CBU images corresponding to different cases. Red and blue fringes are clearly visible in the 120 Hz AMLCDs, while they are greatly suppressed in the 600 Hz AMLCDs. To quantify the difference

between the CBU images and the original image, we adopt the CIEDE2000 color difference as a metric and average the CIEDE2000 color difference values of all pixels to obtain a CBU value. Corresponding to 120 Hz, 300 Hz, and 600 Hz AMLCDs, the calculated CBU values are 4.53, 1.84, and 0.93, respectively. A smaller CBU value represents a higher similarity to the original image and thereby a smaller CBU. On the other hand, various decomposition algorithms have been proposed, such as a three-field Stencil algorithm. Conventional RGB FSC display decomposes an image into three subframes where the individual RGB backlight is turned on in the first, second, and third subframe, respectively. Compared to RGB FSC, the Stencil method adopts a multi-color image as the first subframe (Figure 3-8). During the first subframe, RGB LEDs are simultaneously turned on to generate high luminance and rough color. In this way, the luminance of the remaining mono-colored subframes is reduced and thus the CBU is suppressed. A multi-color image requires a mini-LED backlight to enable local dimming. The backlight intensities of RGB LEDs are obtained by averaging the RGB components of pixel values in each dimming zone, respectively. Then the LC transmittance can be determined according to dividing the pixel value by the backlight intensity. Nevertheless, the image distortion can be noticeable in the corners of the “CREOL” logo (Figure 3-8) because of the clipping effect. With 300 Hz AMLCDs (simultaneous emission), three-field Stencil can lead to a CBU value of 1.60, which is lower than 1.84 (RGB FSC) but is higher than 0.93 (600 Hz AMLCDs with progressive emission).

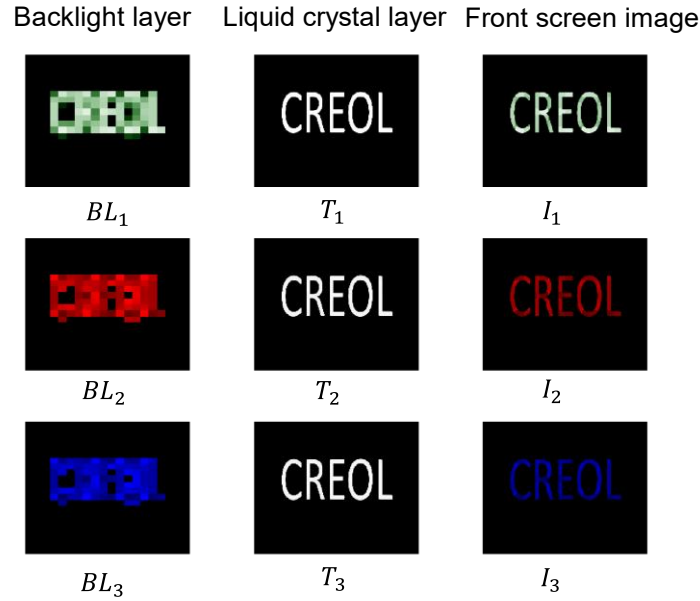


**Figure 3-8 The simulated three-field Stencil algorithm including the simulated backlight layers, liquid crystal layers and front screen images.**

In addition to evaluating the CBU of FSC LCDs, contrast ratio, color gamut, and color shift are sequentially simulated. Light engines play a significant role in determining system contrast ratio. Because of the depolarization from TFT circuits, LCs, and color filters, the contrast ratio of the FFS mode is limited to  $\sim 2500:1$ . For this reason, the FSC LCD can exhibit a higher contrast ratio by eliminating color filters. We use a positive A-plate and negative A-plate as compensation films. [Figure 3-9](#) depicts the simulated isocontrast contour at  $\lambda = 550$  nm. A high contrast ratio ( $\sim 1000:1$ ) region expands to  $\sim 20^\circ$  viewing cone, which is usually adequate for VR applications. Color gamut and color uniformity are also critical to the performance of light engines. In the Meta Quest Pro, quantum dots (QDs) are used in the LCD's backlight module. Therefore, we compare the FSC LCD using RGB LEDs [37] with the LCD using a QD color conversion layer and pigment color filters [38] in terms of color gamut and color shift.

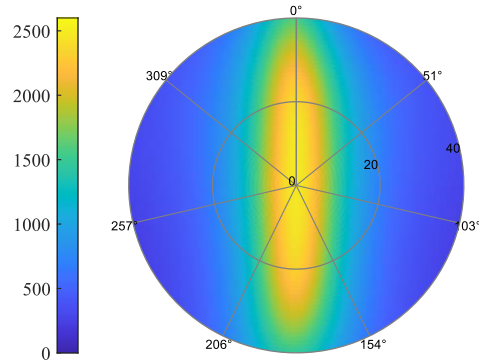


**Figure 3-9 Simulated isocontrast contour for single-domain FFS mode using TechWiz software. The operating temperature is 50 °C.**

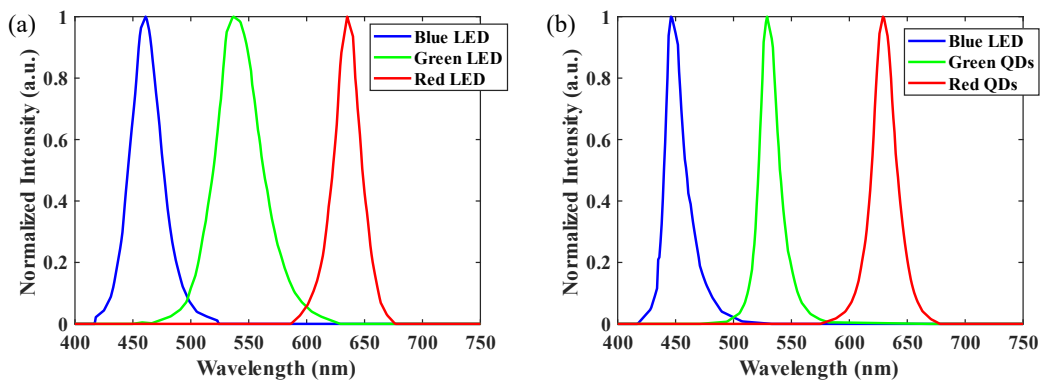


**Figure 3-10 The spectra used in (a) FSC LCD with RGB LEDs, and (b) a blue LED, green QDs, and red QDs in the backlight module of the LCD with the QD enhancement film.**

Figure 3-10(a) shows the spectra of RGB LEDs used in the FSC LCD; while Figure 3-10(b) depicts the spectra of a blue LED, green QDs, and red QDs employed in the backlight module of the LCD. The color gamut of FSC LCDs is mainly limited by the broader emission spectrum of the green LED, as shown in Figure 3-10(a). For an InGaN-based LED, its spectral bandwidth increases as the peak emission wavelength increases because of the increased indium concentration. In contrast, the red-color III-phosphides LEDs exhibit a relatively narrow spectral bandwidth and high efficiency. For the color filter-based LCD, the crosstalk caused by the overlap between the backlight's spectrum in Figure 3-10(b) and color filters hinders a wider

color gamut. Therefore, their color gamut is comparable: the FSC LCD can cover 96.2% DCI-P3 while the LCD using color filters can cover 96.4% DCI-P3. The color gamut of the FSC LCD can be further enlarged using a green LED with a narrower emission spectrum. Incomplete switching of the LC can cause the shrinkage of color gamut; thus, a larger color gamut also helps mitigate the demanding requirement of LC response time.

For color shift, the horizontal ( $\phi = 0^\circ$ ) and vertical ( $\phi = 90^\circ$ ) viewing directions are usually reported experimentally. To calculate color shift, we first extracted wavelength- and angle-dependent transmittance from TechWiz and then multiplied it by the backlight's spectrum and the transmittance spectra of color filters. [Figures 3-11\(a\)](#) and [3-11\(b\)](#) show the simulated color shift for FSC LCD and LCD with color filters, respectively. In both types of LCDs, blue colors in the vertical direction have the largest color shift ( $\Delta u'v'$ ), and then followed by green and red. We also find that the FSC LCD exhibits a  $\sim 3x$  smaller color shift than the LCD with color filters. To summarize, by our calculations, the FSC LCD is proven to exhibit a wide color gamut and superior color uniformity than the LCD with QDs and color filters. It is noted that when  $\Delta u'v'$  is smaller than 0.02, the color shift is indistinguishable to human eyes. Therefore, both types of LCDs are fine in terms of color shift.

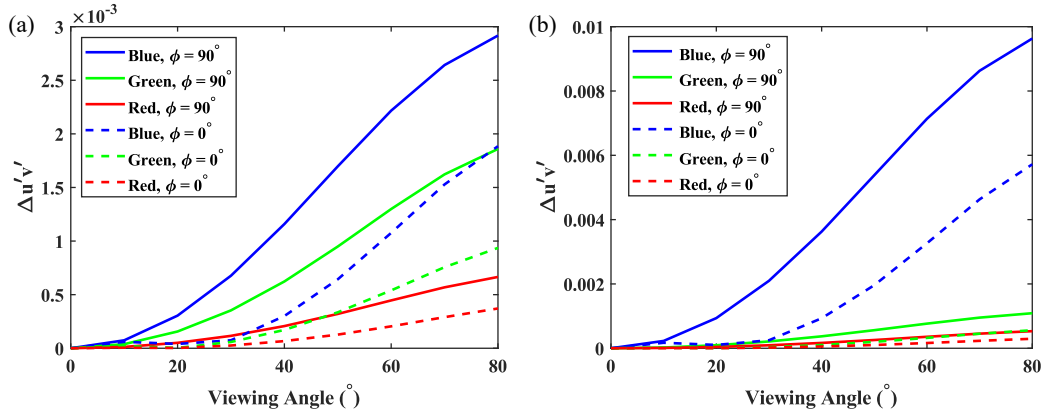


**Figure 3-11 Simulated color shift versus viewing angles for RGB wavelengths at horizontal (dashed lines) and vertical direction (solid line), respectively, for (a) FSC LCD with RGB LEDs, and (b) color filter-based LCD with a QD enhancement film.**

### 3.4 Discussions

Through eliminating color filters, both spatial resolution and optical efficiency can be tripled, but the shorter capacitor charging/discharging time need to be considered as well. Because of the reduced turn-on time, LED backlights should be optimized to generate the required peak brightness. Multistring LED backlight driving system [39] was proposed to alleviate the requirement for a higher peak power and reduce power consumption. On the other hand, the shorter capacitor charging time will slightly lower the transmittance, but the  $\sim 3x$  optical gain may compensate for the decreased transmittance. Also, scanning the gate lines simultaneously can restore to an original charge time without FSC. The increased cost will still be much cheaper than micro-OLEDs using a whole silicon wafer. Another strategy is to employ TFTs with a higher mobility and thereby to reduce the time constant of the capacitor.

As for contrast ratio, the mini-LEDs can be employed to increase the contrast ratio of the LCD. With the help of mini-LEDs, the vertical alignment (VA) mode will not outperform the

FFS mode in terms of contrast ratio. Also, it is challenging to obtain such a fast response time using VA mode. Besides response time, viewing angle is another concern for VA mode. Negative c-plate compensation films may be introduced to widen the viewing cone of VA mode. On the positive side, the VA mode with incident circularly polarized light can exhibit a much higher transmittance than the FFS mode using zero rubbing angle. Overall, the FFS FSC-LCD using a locally dimmable mini-LED backlight is a strong contender for VR displays.

### 3.5 Summary

One of the biggest hurdles for immersive VR is screen-door effect, which arises from insufficient resolution density of VR displays. In other words, the pixel structure including black matrices may be visible because of the magnification from the lens if the resolution density is not high enough. To solve this tough problem, we propose an FSC LCD to achieve 60 PPD and 100° FoV while keeping a low power consumption for compact VR displays. To prove concept, in experiment we reported and evaluated a new high birefringence nematic LC mixture. Our simulation results show that the average GTG response time can be as fast as ~ 1.5 ms to avoid color breakup. Combining our fast-response LC material and structure with progressive emission enabled by mini-LEDs, we demonstrate that a refresh rate of 600 Hz is feasible. By quantitative calculations, we have proven that the CBU can be well suppressed with such a high refresh rate. The FSC LCD also exhibits a high contrast ratio, superior color uniformity, and wide color gamut. It is expected that our proposed and designed high framerate FSC LCD will be a strong contender for high-end VR displays in the future.

## CHAPTER 4: TANDEM WHITE MICRO-OLEDs FOR VR DEVICES

### 4.1 Background

Organic light-emitting diodes (OLED) have been widely used in flat panel displays ranging from smartphones to televisions. With the rapid development of augmented reality (AR) and virtual reality (VR), conventional active-matrix OLED on glass substrates cannot meet the requirement for high resolution density because multiple thin film transistors (TFTs) are employed in each pixel. To greatly increase the resolution density, OLED-on-silicon (also called micro-OLED; OLED microdisplay) has been developed via depositing organic molecules on top of a crystalline silicon CMOS backplane instead of glass substrates. According to the front plane, micro-OLED can be categorized into white OLEDs (WOLEDs) with patterned color filters, and patterned RGB OLEDs. The former eases the manufacturing processes because the resolution density is determined by color filters that can be fabricated by mature photolithography methods, while the latter usually requires a fine metal mask (FMM) to define the RGB sub-pixels. However, it is challenging to fabricate small-pitch ( $< 10\text{-}\mu\text{m}$ ) FMMs because of the shadow effect. Compared to liquid crystal displays (LCDs), micro-OLED exhibits a higher resolution density, higher contrast ratio, fast response time and smaller form factor. In this chapter, we will focus on improving the performance of WOLED microdisplay in a pancake VR system.

Due to its better stability, most of the present commercial WOLED products employ the blue fluorescence emitters and yellow, green, or red phosphorescent emitters, which are named as hybrid WOLEDs. [Figure 4-1](#) shows typical device structures of WOLEDs with different numbers of stacks and colors. The simplest architecture is single-stack WOLED shown in [Figure 4-1\(a\)](#). It consists of a reflective anode, a hole injection layer (HIL), a hole transport layer (HTL),

emission layers (EMLs), an electron transport layer (ETL), an electron injection layer (EIL), and a cathode. White light is generated via the combination of a blue emission layer (EML), a green EML, and a red EML, which Sony demonstrated in 2019 [40]. Compared to common single-stack WOLED displays ( $\sim 2$  cd/A), Sony employed an InZnO cathode, a microlens array, and optimized color filters to achieve a current efficiency of 6 cd/A and a color gamut of 108% sRGB. Despite its simple architecture, the efficiency and lifetime of the single-stack WOLED microdisplay remain to be improved because only about 25% of the white light transmits through the color filters.

To improve the efficiency and lifetime, tandem WOLEDs [41] have been proposed. They are constructed by two or more EMLs that are connected by charge generation layers (CGLs). The CGL usually consists of a n-p semiconductor heterojunction layer [42], responsible for charge generation. The p-CGL and n-CGL should exhibit low operating voltage, efficient charge generation, high transparency, excellent conductivity, and good thermal stability. Therefore, engineering CGL materials is critical for high-performance tandem WOLEDs [43]. [Figures 4-1\(b-e\)](#) show various architectures of tandem WOLEDs. The 2-stack tandem WOLED is shown in [Figures 4-1\(b\) & 4-1\(c\)](#). In comparison with single-stack WOLED, the 2-stack WOLED consists of two spatially separated recombination zones by a CGL. By doing so, one electron-hole pair can generate photon twice, doubling the current efficiency. Furthermore, two spatially separated recombination zones enable different EMLs to be placed in the respective antinode positions, where the light wave emitted from the EML is constructively interfered to maximize the light extraction efficiency. The thinnest tandem WOLED device can be obtained via locating all the EMLs at the respective first antinodes, contributing to reducing the driving voltage [44]. Kopin

demonstrated a 2-stack WOLED microdisplay with an average current efficiency of 12 cd/A [45]. The more than twice improvement arises from material selections and optimal cavity designs. The boosted efficiency enables WOLEDs to achieve a much higher luminance at the same current, or a much longer lifetime at the same luminance. The tradeoff of tandem WOLEDs is the increased operating voltage and increased material costs owing to additional CGLs and EMLs. Efficient electron injection and hole injection help lower the operating voltage of tandem WOLEDs. For example, Cho et al. reported a 2-stack 2-color tandem WOLED with the n-doping ETL and p-doping HIL to lower the operating voltage [46]. To enhance the color performance, we can replace the yellow EML with a red EML and a green EML, as shown in [Figures 4-1\(c\) & 4-1\(d\)](#). The operating voltage may increase because of an additional EML or an additional stack. To further improve the efficiency of the 2-stack tandem WOLED, we can use three stacks consisting of two blue EMLs and a unit including red and green EMLs ([Figure 4-1\(d\)](#)). For example, Song et al. demonstrated a 3-stack WOLED with wide color gamut and high efficiency [47], and in 2024 LG Display also reported a 3-stack WOLED to obtain a higher current efficiency than the 2-stack WOLED. To generate white emission, we can also use a single EML consisting of a host doped with various color guests [48], which requires precise doping engineering. Likewise, we can use two white EMLs and a CGL to constitute a 2-stack tandem WOLED and thereby to enhance the efficiency, as shown in [Figure 4-1\(e\)](#). It is noted that more stacks (> 3 stacks) can be connected by CGLs to further improve the efficiency, as demonstrated by OLEDWorks [49], but the voltage range of the CMOS backplane may pose a constraint on the number of stacks, which is different from television or automotive applications [50].

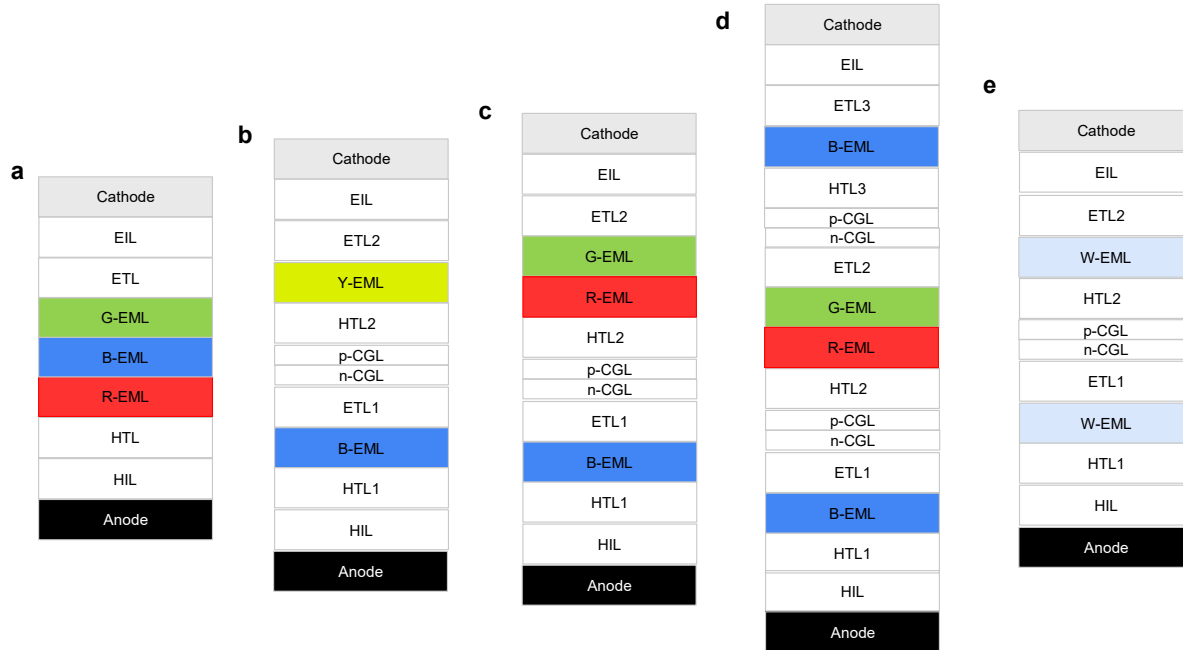


**Figure 4-1 Various device architectures of WOLEDs. (a) 1-stack 3-color WOLED architecture, in which white light is generated by the combination of three EMLs. (b) 2-stack 2-color tandem WOLED architecture, in which white light is generated by the combination of two EMLs that are connected by a CGL. (c) 2-stack 3-color tandem WOLED architecture, in which white light is generated by the combination of three EMLs that are connected by a CGL. (d) 3-stack 3-color tandem WOLED architecture, in which white light is generated by the combination of four EMLs that are connected by two CGLs. (e) 2-stack 2-white tandem WOLED architecture, in which two white EMLs are connected by a CGL.**

Considering the balance between the driving voltage and current efficiency, we adopt a 2-stack tandem WOLED structure in this chapter. Despite a higher efficiency enabled by tandem structures, it is currently insufficient for AR applications because of a required ultrahigh brightness. For those reasons, we mainly investigate 2-stack tandem WOLEDs for VR applications. In addition to high efficiency, color fidelity is also critical for VR applications. Owing to the wide emission spectra and crosstalk of the employed color filters, the color gamut of WOLEDs is usually smaller than 100% DCI-P3 (e.g. Apple Vision Pro has a color gamut of 92% DCI-P3). To break the color gamut limit, we propose to combine microcavity tandem

WOLED with high-order antinodes and optimize the VR system. The 2-stack tandem WOLED microdisplay and pancake VR optical system will be modelled, forming the basis for optimization processes. All calculations regarding the entire system are implemented using home-made MATLAB codes.

#### 4.2 Tandem white micro-OLED

The performance of the WOLED microdisplay (white micro-OLED) is determined by several factors such as the thin metal film (semitransparent cathode), capping layer, the numbers, and positions of the EMLs, and color filters, as shown in [Figure 4-2](#). For this reason, the WOLED microdisplay should be well optimized. On the other hand, the optimization target also depends on the optical systems that refract the light emitted from display panels because the display performance in a VR system is jointly determined by the display panel and the optical system [51,52]. To break the color gamut limit and achieve the largest color gamut, we leverage microcavities via introducing different optical cavity lengths for the red, green, and blue subpixels [53] and propose high-order antinodes. More specifically, indium tin oxide (ITO) or hole injection layer (HIL) can be patterned below the common EMLs, as shown in [Figure 4-2](#). Leveraging microcavity effects, we can tune the ITO/HIL thickness to achieve desired narrow spectra before the light transmits through color filters.

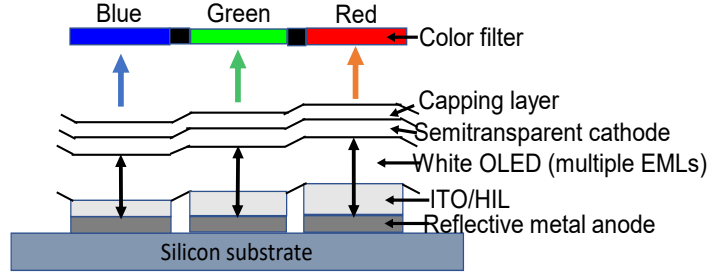


**Figure 4-2 The schematic of tandem WOLED microdisplay with a patterned ITO or HIL layer below the common EMLs.**

To quantify the performance of such a proposed structure in a VR system, total light efficiency ( $TLE$ ), color gamut coverage ( $CGC$ ), and color nonuniformity are considered.  $TLE$  is the product of following three parameters: external quantum efficiency ( $EQE$ ), optical transmission efficiency of color filters ( $\eta_{CF}$ ), and optical system efficiency ( $\eta_{OSE}$ ), as shown in Equation 4-1:

$$TLE = EQE \cdot \eta_{CF} \cdot \eta_{OSE} = (\eta_{OCE} \cdot IQE) \cdot \eta_{CF} \cdot \eta_{OSE}, \quad (4-1)$$

where  $EQE$  is the product of outcoupling efficiency ( $\eta_{OCE}$ ) and internal quantum efficiency ( $IQE$ ). The outcoupling efficiency can be calculated by the rigorous dipole model. The transmission efficiency of color filters can be calculated using Equation 4-2:

$$\eta_{CF} = \frac{\iint K(\theta, \lambda) \cdot T_{CF}(\lambda) d\theta d\lambda}{\iint K(\theta, \lambda) d\theta d\lambda}, \quad (4-2)$$

where  $K(\theta, \lambda)$  is the power dissipation density corresponding to different emission angles and wavelengths, and  $T_{CF}(\lambda)$  is the transmission spectra of color filters. A higher transmission efficiency will contribute to a higher  $TLE$ . Equation 4-3 shows how to calculate the optical system efficiency ( $\eta_{OSE}$ ):

$$\eta_{OSE} = \frac{\iint (\int K(\theta, \lambda) \cdot T_{CF}(\lambda) \cdot d\lambda) \sin(\theta) \cdot \eta_c(\theta, p) d\theta dp}{\iint (\int K(\theta, \lambda) \cdot T_{CF}(\lambda) \cdot d\lambda) \sin(\theta) d\theta dp}, \quad (4-3)$$

where  $\eta_c(\theta, p)$  is the collection efficiency depending on the emission angle and the location of the point source, which is calculated as the ratio of power collected by the eye pupil to the power emitted from the point source. According to Equation 4-3,  $\eta_{\text{ose}}$  is impacted by the emission cone of display panels and the collection cone. The emission cone is usually much larger than the collection cone, thus leading to low optical system efficiency. Thus, a moderate or strong microcavity helps narrow down the angular distributions of the emitting pixels and thereby increase the optical efficiency. To quantify the color performance in a VR system, the position-dependent spectrum is defined in Equation 4-4:

$$S(\lambda, p) = \int K(\theta, \lambda) \cdot T_{CF}(\lambda) \cdot \sin(\theta) \cdot \eta_c(\theta, p) d\theta \quad (4-4)$$

Then, the CGC of the central pixel ( $p = 0$ ) is defined in Equation 4-5:

$$CGC = \frac{A_{\text{display}} \cap A_{\text{standard}}}{A_{\text{standard}}}, \quad (4-5)$$

where  $A_{\text{display}}$  is the triangular area of the display whose three vertices are color coordinates calculated from  $S_{\text{red}}(\lambda, 0)$ ,  $S_{\text{green}}(\lambda, 0)$ , and  $S_{\text{blue}}(\lambda, 0)$ , respectively, and  $A_{\text{standard}}$  is the triangular area of the reference standard (DCI-P3 or Rec. 2020). Stronger microcavities help narrow the emission spectra, leading to a larger CGC. But the TLE may decrease and the color nonuniformity may increase. Lastly, the color nonuniformity is defined as the color difference between the central pixel and the neighboring pixels. Considering color mixing, the maximum color nonuniformity of the first 18 colors in Macbeth Color Checker is defined as the color nonuniformity in a VR system. For a tandem WOLED, the TLE, CGC, and color nonuniformity can be obtained by incoherently superimposing the power dissipation density  $K$  of randomly oriented dipoles in different EMLs.

### 4.3 Pancake optical system

Pancake lens has become the mainstream of VR headsets because of its compactness [7]. Here, we build a raytracing model in the LightTools software, as shown in [Figure 4-3](#). In this model, the distance from display to the lens is 16.4 mm, the diameter of the lens is 41.2 mm, and the eye relief is 13.3 mm. We model the display panel using 20-point sources with a 1-mm spacing, which can achieve a  $\sim 100^\circ$  horizontal field of view with the magnification of the pancake lens. The diameter of the eye pupil is 4 mm. The reflective circular polarizer can be made of a broadband quarter-wave plate and a reflective linear polarizer or just using a cholesteric liquid crystal film. In our model, a broadband quarter-wave plate and a reflective polarizer based on multilayer thin films are employed to function as a reflective circular polarizer. [Figure 4-4](#) depicts the collection efficiency depending on the emission angle and the location of the point source. The maximum collection efficiency of  $\sim 12.5\%$  is attributed to the 50% absorption loss of a circular polarizer placed in front of the point sources and the 75% loss from traversing through the half mirror twice. As a comparison, if we adopt a wire grid polarizer to act as reflective linear polarizer, the maximum collection efficiency is reduced to  $\sim 10\%$  owing to its intrinsic absorption. On the other hand, the collection cone for almost all pixels falls within  $\sim 5^\circ$ , arising from a telecentric design of the pancake lens and a small eye pupil.

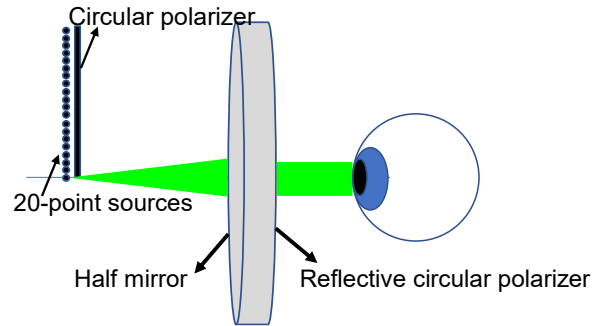


**Figure 4-3** The schematic of a pancake VR system consisting of a circular polarizer, a half mirror, and a reflective circular polarizer.

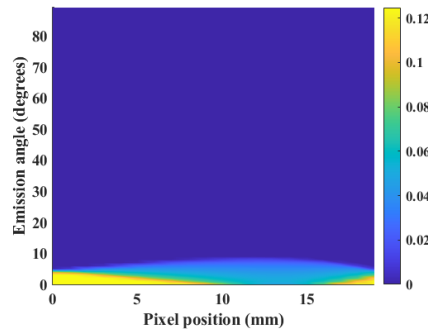


**Figure 4-4** The collection efficiency depending on the emission angle and the location of the point source.

#### 4.4 Analysis and optimization

Based on [Figure 4-2](#), the layer from the bottom to the top can be listed as follows: CMOS/Ag/ITO/HIL/HTL/B-EML/CGL/Y-EML (or other EMLs)/ETL/Cathode (thin Mg:Ag alloy) /Capping. Different EMLs are connected in series with a charge generation layer (CGL). The thickness of the Ag layer is 100 nm to provide a high reflection. All the EML thicknesses are 10 nm, and the thickness of the electron transport layer (ETL) is 30 nm. If HIL is patterned to introduce different optical cavity lengths, the ITO thickness is fixed at 10 nm. If ITO is patterned, the HIL thickness is fixed at 20 nm. To perform system-level analysis and optimization, we introduce five independent variables, which can be denoted by  $D = [d_1, d_2, d_3,$

$d_4, d_5]$ . More specifically,  $d_1, d_2$ , and  $d_3$  are the HIL or ITO thicknesses corresponding to blue, green, and red subpixels, respectively,  $d_4$  is the cathode thickness, and  $d_5$  is the capping thickness. The former three variables  $[d_1, d_2, d_3]$  mainly modulate the radiated intensity of multiple emissive layers; the latter two variables  $[d_4, d_5]$  mainly impact the resonance strength and the efficiency. For  $[d_4, d_5]$ , we set  $d_4 \in [10 \text{ nm}, 25 \text{ nm}]$  and  $d_5 \in [0 \text{ nm}, 80 \text{ nm}]$ , respectively. Lastly, our optimization target is to find the maximum  $TLE$  while keeping a color gamut coverage of no less than 99% DCI-P3 and the color nonuniformity  $\Delta u'v' \leq 0.02$  [54]. Considering three subpixels, the  $TLE$  is calculated as the averaged efficiency of three subpixels. We also investigate how wide the color gamut can be since a larger color coverage leads to a better color saturation.

First, we study the simplest tandem structure: B/YG WOLED. It usually exhibits a lower driving voltage than that with more emissive layers. In the blue subpixel, the microcavity should be designed to obtain constructive interference for blue light and destructive interference for yellow-green light. To achieve a minimum thickness, we can locate the blue emitter around the first antinode of the reflective metal electrode and the yellow-green emitter around the first node of the reflective metal electrode. Therefore, the spacing between the two EMLs and the CGL thickness can be calculated, which are approximately 90 nm and 80 nm, respectively. Owing to the CGL thickness, it is not possible to achieve the first antinode corresponding to the yellow-green emitter and thus the second antinode can be employed. By physical analysis, we choose  $d_1 \in [5 \text{ nm}, 35 \text{ nm}]$ ,  $d_2 \in [40 \text{ nm}, 80 \text{ nm}]$ , and  $d_3 \in [85 \text{ nm}, 120 \text{ nm}]$  as boundary constraints. In the following, we use green subpixel as a preliminary demonstration because it greatly determines how wide the color gamut can be.

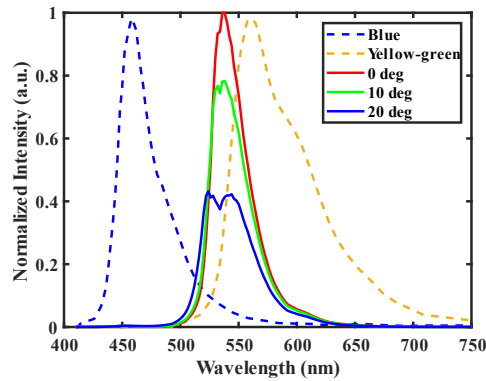


**Figure 4-5 The spectra of the green subpixel at different angles: 0 deg, 10 deg, and 20 deg. The emission spectra of blue and yellow-green emitters are also shown.**

Figure 4-5 shows the spectra of the green subpixel corresponding to different angles, as indicated by solid lines. As a reference, the emission spectra of the blue (BPP<sub>y</sub>A) and yellow-green (Ir(tp<sub>2</sub>tpy)<sub>2</sub>acac) emitters are also included using dashed lines. If  $d_2$  (HIL) = 60 nm,  $d_4$  = 25 nm, and  $d_5$  = 60 nm, we can obtain the spectrum with a central wavelength of 538 nm and the full width at half maximum (FWHM) = 32 nm. Such a narrow FWHM arises from the strong microcavity. If ITO is selected to control the cavity length corresponding to the green subpixel, we can calculate  $d_2$  (ITO) = 50 nm to achieve a similar result to Figure 4-5. To investigate how  $d_2$  and  $d_4$  impact the transmitted spectrum, we calculate the spectra and color coordinates corresponding to different values for  $d_2$  and  $d_4$ . As Figure 4-6 depicts, a thicker Mg:Ag film helps achieve DCI-P3's green primary given a certain  $d_2$ . Besides color coordinates, position-dependent color shift corresponding to different  $d_2$  is simulated, as shown in Figure 4-7. For the source (pixel) positions ranging from 10 mm to 15 mm, the maximum color shift occurs. This is because the maximum collection efficiency corresponding to those pixel positions occurs at larger emission angles ( $\sim 10^\circ$ ) as shown in Figure 4-4, leading to a larger color shift.

According to this demonstration, it is feasible to eliminate the green color filter because the

blue light can be almost suppressed by deconstructive interference at a certain condition. The same conclusion also applies to the blue subpixel because of destructive interference of yellow-green light. Although color filters help increase ambient contrast ratio, this advantage may disappear because we can laminate another quarter-wave plate onto the circular polarizer to eliminate the reflected light from half mirror. Compared to blue and green subpixel, it is more challenging to eliminate the red color filter. In a red subpixel, we would like to locate the yellow-green emitter around the second antinode for a resonance wavelength of  $\sim 630$  nm. Unfortunately, the blue emitter is simultaneously located closer to the second antinode for a resonance wavelength of  $\sim 460$  nm. For this reason, dual peaks emerge in the red subpixel. To improve optical efficiencies of the blue and green subpixels and achieve a decent color gamut, we can just pattern the red color filters.

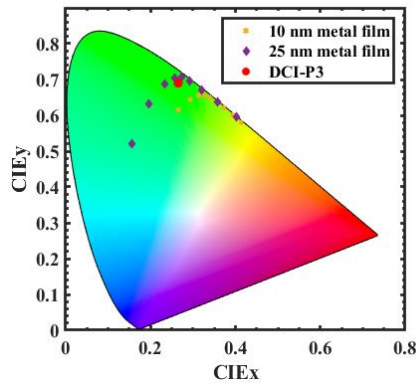


**Figure 4-6 The CIE 1931 coordinates of the green subpixel as a function of  $d_2$  at  $d_4 = 10$  nm and  $d_4 = 25$  nm, respectively.**

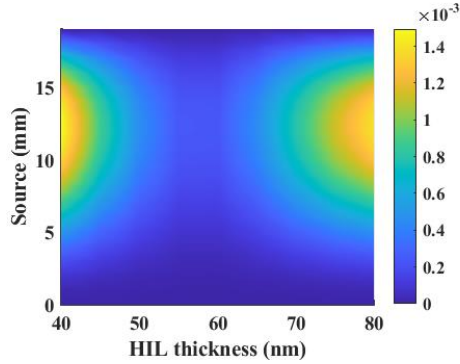


**Figure 4-7 Simulated color shift of the green subpixel corresponding to different source positions and HIL thicknesses ( $d_2$ ).**

As mentioned before, we can achieve DCI-P3's green primary with the low-order antinodes with a strong microcavity; however, the efficiency is inevitably reduced owing to the larger absorption of the metal cathode. According to the principles of interference, a longer cavity length contributes to generating the spectrum with a narrower FWHM. Therefore, we propose a B/YG WOLED with the high-order antinodes to improve the color gamut and efficiency. We repeat the same optimization process as the low-order antinodes except that  $d_1 \in [110 \text{ nm}, 150 \text{ nm}]$ ,  $d_2 \in [160 \text{ nm}, 200 \text{ nm}]$ ,  $d_3 \in [230 \text{ nm}, 280 \text{ nm}]$ , and the CGL thickness is 110 nm. Compared to the low-order antinodes, we locate the blue emitter around the second antinode of the reflective metal electrode and the yellow-green emitter around the second node of the reflective metal electrode. The optimized result shows that the maximum color gamut can increase from 80% to 92% of Rec. 2020. Also, the layer thicknesses for optimal solutions corresponding to the low-order antinodes and high-order antinodes are  $D_l = [25 \text{ nm}, 55 \text{ nm}, 115 \text{ nm}, 20 \text{ nm}, 80 \text{ nm}]$  and  $D_h = [120 \text{ nm}, 180 \text{ nm}, 255 \text{ nm}, 15 \text{ nm}, 80 \text{ nm}]$ , respectively. The corresponding optimal  $TLE$  is  $1.39 \times 10^{-4}$  and  $2.26 \times 10^{-4}$ , respectively. The 62% improvement mainly arises from the reduced cathode thickness ( $d_4$ ) required to achieve a color gamut of no

less than 99% DCI-P3. It is noted that a higher-order antinode helps further to widen the color gamut, but the efficiency may be reduced, and the conductivity could be an issue.

Then we investigate another tandem structure: B/G/R WOLED. We input the emitted spectra from three EMLs and then repeat the same optimization procedures as the B/YG WOLED. [Figure 4-8](#) manifests the comparison of color gamut coverages between the B/YG and B/G/R WOLED with the low-order antinodes. When  $D_l = [20 \text{ nm}, 55 \text{ nm}, 120 \text{ nm}, 25 \text{ nm}, 0 \text{ nm}]$ , 100% DCI-P3 or 80% Rec.2020 can be achieved via B/YG. To achieve a much wider color gamut, deep green with a high CIE  $y$  value is highly desired. With a green EML and a designed cavity, B/G/R-v2 and B/G/R-v1 can achieve a color gamut of 95% and 90% Rec.2020, respectively, when  $D_l = [10 \text{ nm}, 50 \text{ nm}, 110 \text{ nm}, 25 \text{ nm}, 0 \text{ nm}]$  and  $D_l = [5 \text{ nm}, 45 \text{ nm}, 120 \text{ nm}, 10 \text{ nm}, 80 \text{ nm}]$ , respectively. To achieve an ultrawide color gamut while keeping a high efficiency, we propose a B/G/R WOLED with the high-order antinodes, just like B/YG WOLED. For example, when  $D_h = [110 \text{ nm}, 165 \text{ nm}, 255 \text{ nm}, 15 \text{ nm}, 0 \text{ nm}]$ , a color gamut with 95% Rec. 2020 can be achieved with a 15-nm cathode. This structure also enables a color gamut of 93% Rec. 2020 with a 10-nm cathode when  $D_h = [110 \text{ nm}, 165 \text{ nm}, 265 \text{ nm}, 10 \text{ nm}, 80 \text{ nm}]$ .

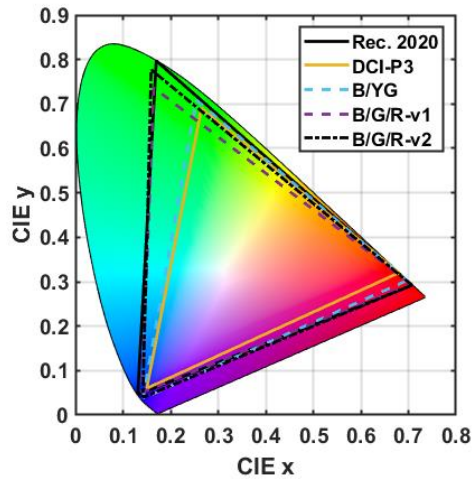


Figure 4-8 (a) Simulated color gamut corresponding to B/YG WOLED and B/G/R WOLED with different  $d_4$  and  $d_5$ .

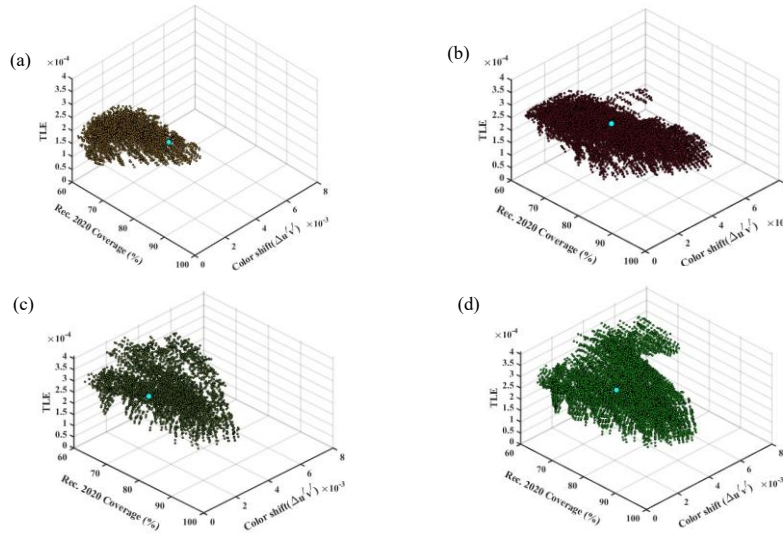


Figure 4-9. Optimization results of WOLED microdisplays: (a) B/YG (b) high-order B/YG (c) B/G/R, and (d) high-order B/G/R. Cyan points represent optimal solutions corresponding to each case.

For B/G/R WOLEDs, the layer thicknesses for optimal solutions corresponding to the low-order antinodes and the high-order antinodes are  $D_l = [5 \text{ nm}, 55 \text{ nm}, 100 \text{ nm}, 10 \text{ nm}, 80 \text{ nm}]$  and  $D_h = [115 \text{ nm}, 175 \text{ nm}, 245 \text{ nm}, 10 \text{ nm}, 80 \text{ nm}]$ , respectively. The corresponding optimal  $TLE$  is

$3.64 \times 10^{-4}$  and  $3.58 \times 10^{-4}$ , respectively. In comparison with B/YG WOLED with the low-order antinodes,  $\sim 160\%$  efficiency improvement is mainly attributed to the 10-nm cathode. All optimal solutions are marked in [Figure 4-9](#).

#### 4.5 Summary

In this chapter, we have modelled the performance of WOLED in pancake VR headsets, forming the basis for systematical analysis and optimization. For both B/YG and B/G/R WOLED, we first analyze the boundary constraints for  $[d_1, d_2, d_3]$  to speed up the simulation process, and then optimize their performances. Our results indicate that it is possible to eliminate the blue and green color filters to improve the optical efficiencies of B/YG WOLED. More importantly, we propose a new structure to combine the high-order antinodes and pattern the microcavities. Our simulation results also indicate that our proposed structure can improve the efficiency of B/YG WOLED by  $\sim 62\%$  at the optimal conditions compared to the B/YG WOLED with the low-order antinodes. It also enables a color gamut coverage of 92% Rec. 2020 in B/YG WOLED with a strong microcavity. For B/G/R WOLED, a color gamut of 95% Rec. 2020 can be achieved with a moderate microcavity.

## CHAPTER 5: SMALL PIXEL-SIZE LCoS FOR AR DEVICES

### 5.1 Background

In a waveguide-based AR system [55], microdisplays act as light engines, which generate image contents that are overlaid with physical worlds via the waveguide combiner. With the development of microdisplay technologies, liquid-crystal-on-silicon (LCoS), digital light processing (DLP), OLED-on-silicon, micro-LED ( $\mu$ LED), and laser beam scanning (LBS) are available microdisplays for the waveguide-based AR. Each microdisplay has its own merits and demerits [56]. The brightness of OLED-on-silicon and the compactness of DLP are critical bottlenecks for their applications to waveguide-based smart glasses.  $\mu$ LED microdisplays require further development on directional angular distribution [57] and small full-color pixel size [58]. LBS needs significant improvements on the frame rate and resolution. Compared to those light engines, LCoS offers great potential for achieving high-efficiency and high-resolution waveguide-based AR displays. Therefore, we will focus on improving the performance of LCoS microdisplay for waveguide-based AR displays.

### 5.2 Small pixel-size LCoS

Amplitude-modulating LCoS utilizes voltage-induced liquid crystal reorientations to modulate the polarization state of the incoming light and pixelated metallic mirrors to reflect the modulated light. Therefore, amplitude-modulating LCoS requires a polarized light, which is different from those polarization-independent liquid crystal devices [59,60]. As a comparison, the phase-only LCoS for holographic displays usually requires a linearly polarized light with modulated pixelated phase change. Fast response time is more challenging in phase LCoS

because of a twice thicker cell gap. Polymer network LC offers a submillisecond response time, but the required driving voltage is much higher [61]. In this chapter, we will focus on amplitude modulating LCoS. Currently, a big challenge for LCoS is to reduce its form factor, which is critically important for waveguide-based AR glasses. To realize this goal, Himax has developed a front lit LCoS. A key element in the front lit LCoS is a flat plate (lightguide) placed on top of the LCoS module. Combined with a reflective polarizer and micro polarizing beam splitter array, the flat plate can eliminate the bulky polarizing beam splitter cube and dramatically reduce the volume of the illumination system. More specifically, the LED is mounted at the edge of the lightguide. A wire grid polarizer is placed between the LED and the lightguide to increase the polarization conversion efficiency. The reflective polarizer is placed on top of the lightguide, which functions as an analyzer. Although the volume is greatly reduced, the brightness of the front lit LCoS needs to be further increased owing to the low efficiency of diffractive waveguides. Another challenge is related to fringing field effect (FFE) when the small pixel size ( $\leq 3 \mu\text{m}$ ) becomes closer to the cell gap ( $\sim 1.5 \mu\text{m}$ ). The fringe field is generated between the voltage-on and the adjacent voltage-off pixels. The disclination lines produced by the fringing field decrease the efficiency and contrast ratio for the amplitude LCoS [62]. The FFE is governed by several factors, such as the LC mode, cell gap, pixel size, and polarization state of the illumination light. Two major LC modes, mixed-mode twisted nematic (MTN) and vertical alignment (VA), have been widely adopted. The VA mode exhibits advantages in high on-axis contrast ratio and insensitivity to the incident wavelength and cell gap. However, the optical efficiency is greatly reduced by the FFE. In contrast, the MTN mode exhibits a weaker FFE. The factors that impact the FFE of the VA mode have been widely explored. For example, circularly

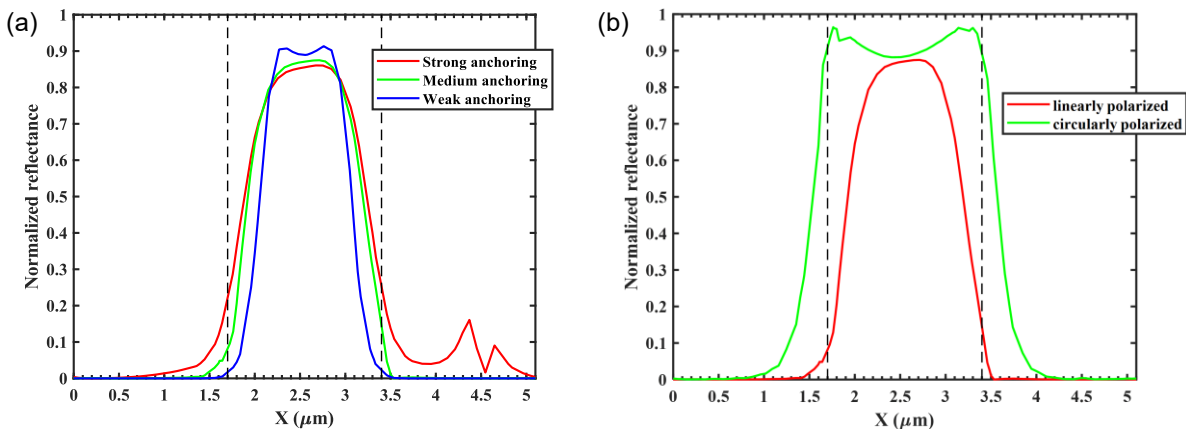
polarized light helps boost the optical efficiency of VA LCoS [63]. Besides, a large pretilt angle helps eliminate the dark stripe. However, the FFE of the MTN mode has not been thoroughly investigated. In this section, we will comprehensively study how device parameters, such as anchoring energy and alignment angle, impact and mitigate the FFE of the MTN mode. Dielectric shielding walls are also proposed to ease the FFE. Mitigating the FFE enables a smaller pixel size, which contributes to a higher resolution density or smaller form factor.

For the MTN mode, the LC directors are twisted by  $90^\circ$  from the bottom substrate to top substrate, which is called  $90^\circ$ -MTN. A relatively high contrast ratio can be obtained due to the built-in phase compensation from the two orthogonal boundary layers. For an incident linearly polarized light, the angle between the polarization direction and the front LC director of the MTN cell is called  $\beta$ , which is usually set at about  $20^\circ$  to maximize the reflectance. Nevertheless, considering the FFE and response time,  $\beta = 0^\circ$  may exhibit a greater advantage because of enabling a thin cell gap. To investigate the effect of anchoring energy on the FFE in the  $1.5\text{-}\mu\text{m}$  pixel-size LCoS panel, we vary the anchoring energy of the  $90^\circ$ -MTN cell with  $\beta = 0^\circ$ , as shown in [Figure 5-1\(a\)](#). As the anchoring energy decreases from  $1 \times 10^{-3} \text{ J/m}^2$  (strong anchoring) to  $1 \times 10^{-5} \text{ J/m}^2$  (weak anchoring), the light leakage (crosstalk ratio) decreases and the peak efficiency increases. This interesting finding suggests a relatively weak anchoring energy for suppressing the pixel crosstalk in the ultrasmall pixel-size MTN LCoS panel. The tradeoff is a slower response time. Therefore, a medium anchoring energy is preferred due to a delicate balance between FFE and response time. Fortunately, the anchoring energy supported by inorganic alignment layers falls into the region of medium anchoring. Another finding is the effect of incident polarization. As shown in [Figure 5-1\(b\)](#), the incident circularly polarized light

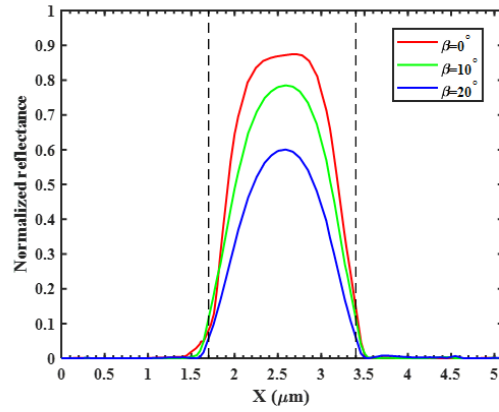
will increase the average efficiency in the bright pixel but the crosstalk ratio as well. Compared to the efficiency gain, a great amount of crosstalk may be unacceptable for practical applications because of potential image blur. To investigate the  $\beta$  angle effect on FFE in the 1.5- $\mu\text{m}$  pixel-size LCoS panel, we vary the  $\beta$  angle to observe the position-dependent reflectance under medium anchoring energy and linearly polarized light conditions. According to Figure 5-2, we can calculate the optical efficiency and crosstalk ratio using Equation 5-1 and Equation 5-2. For those three angles, their crosstalk ratios are almost identical, but their optical efficiencies are greatly different:  $\beta = 0^\circ$  exhibits an optical efficiency of 66%. Compared to VA mode with the same cell gap of 1  $\mu\text{m}$ ,  $\beta = 0^\circ$  exhibits the lowest crosstalk ratio of 1.71%, and a much larger optical efficiency than the VA mode with an linearly polarized incident light (43% optical efficiency).

$$F = \frac{1}{S} \int R_{\text{bright}} \quad (5-1)$$

$$R_{\text{crosstalk}} = \frac{\int_S R_{R\text{-dark}} + \int_S R_{L\text{-dark}}}{\int_S R_{\text{bright}} + \int_S R_{R\text{-dark}} + \int_S R_{L\text{-dark}}} \quad (5-2)$$

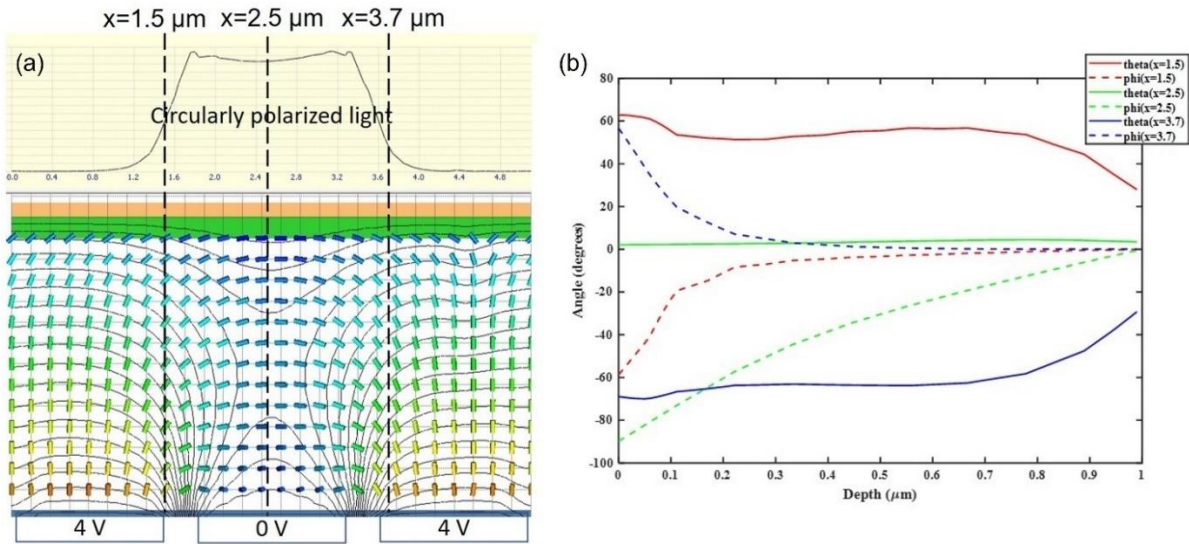


**Figure 5-1 (a) The normalized reflectance as a function of the position at (a) different anchoring energies, and (b) different incident polarization states (linearly polarized and circularly polarized light).**



**Figure 5-2** The normalized reflectance as a function of the position at three  $\beta$  angles:  $0^\circ$ ,  $10^\circ$ , and  $20^\circ$ .

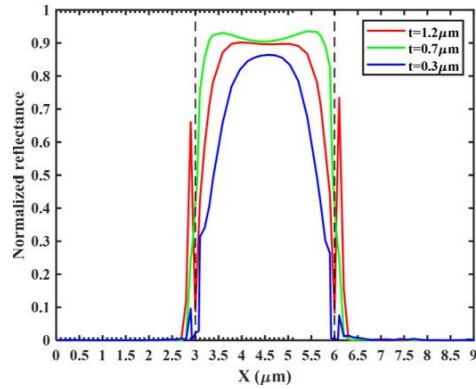
To understand how a circularly polarized light impacts the FFE of the MTN mode, we simulated the distribution of LC directors, as shown in [Figure 5-3\(a\)](#). Because of fringe fields and the positive dielectric anisotropy, the tilt angles of LC directors at the edges of the dark pixels are in the range of  $60^\circ$  to  $70^\circ$  (absolute value) instead of  $90^\circ$ . Also, most of their azimuthal angles are within  $5^\circ$  (absolute value), which are nearly parallel to the horizontal ( $x$ ) axis. For better illustration, we plot the depth-dependent tilt and azimuthal angles of LC directors located at three horizontal positions:  $x = 1.5 \mu\text{m}$  (in the left pixel),  $x = 2.5 \mu\text{m}$  (in the middle pixel), and  $x = 3.7 \mu\text{m}$  (in the right pixel), as shown in [Figure 5-3\(b\)](#). At  $x = 2.5 \mu\text{m}$ , the tilt angles of LC directors are equal to the pretilt angle of  $2^\circ$ , and their azimuthal angles vary from  $-90^\circ$  to  $0^\circ$  as the depth increases from 0 to  $1 \mu\text{m}$ . At  $x = 1.5 \mu\text{m}$  or  $x = 3.7 \mu\text{m}$ , the circularly polarized light can lead to a larger phase retardation or polarization change than the linearly polarized light because it is independent of the azimuthal angles of LC directors, and the tilt angles of LC directors are not  $90^\circ$ .



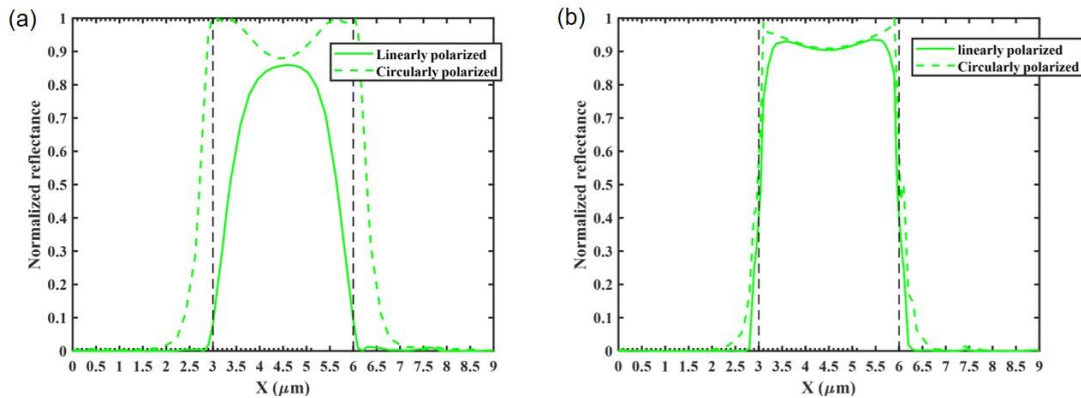
**Figure 5-3 (a) The director distribution in MTN LCoS with 1.5- $\mu\text{m}$  pixel size (the pixel gap is 0.2  $\mu\text{m}$ ) (b) the depth-dependent tilt and azimuthal angles of LC directors located at three different horizontal ( $x$ -axis) positions: 1.5  $\mu\text{m}$ , 2.5  $\mu\text{m}$ , and 3.7  $\mu\text{m}$ .**

Dielectric shielding walls have been explored in the LCoS phase modulator [64]. To further reduce the FFE of a MTN LCoS, we propose to introduce shielding walls to MTN LCoS amplitude modulator. Figure 5-4 shows the position-dependent reflectance corresponding to shielding walls with three different heights: 0.3  $\mu\text{m}$ , 0.7  $\mu\text{m}$ , and 1.2  $\mu\text{m}$ . The pixel pitch is 3  $\mu\text{m}$ , which is currently manufacturable. From simulation results, an optimal thickness of 0.7  $\mu\text{m}$  is found, which greatly mitigates the FFE and thereby supports a nearly square profile. The width of shielding walls is equal to the pixel gap of 0.2  $\mu\text{m}$ , which keeps the aperture ratio unchanged. On the other hand, the aspect ratio of shielding walls with 0.7- $\mu\text{m}$  thickness is 3.5:1, which greatly ease the fabrication difficulty. As mentioned above, circularly polarized light can lead to greater crosstalk in the MTN LCoS because of the horizontal fringe fields. To validate this finding, we simulate the position-dependent reflectance corresponding to a linearly polarized light and a circularly polarized light, and then compare their results: a) without shielding walls,

and b) with shielding walls. The result without shielding walls is shown in Figure 5-5(a). The FFE has a great dependency on the incident light polarization when strong fringe fields are induced. Figure 5-5(b) demonstrates that the reflectance profiles corresponding to linearly polarized light and circularly polarized light are almost identical when the horizontal fringe fields are greatly suppressed by shielding walls. Shielded fringe fields help restore the tilt angles of LC directors at the edges of dark pixels to nearly  $90^\circ$ . Therefore, the polarization dependency of phase retardation is greatly mitigated.



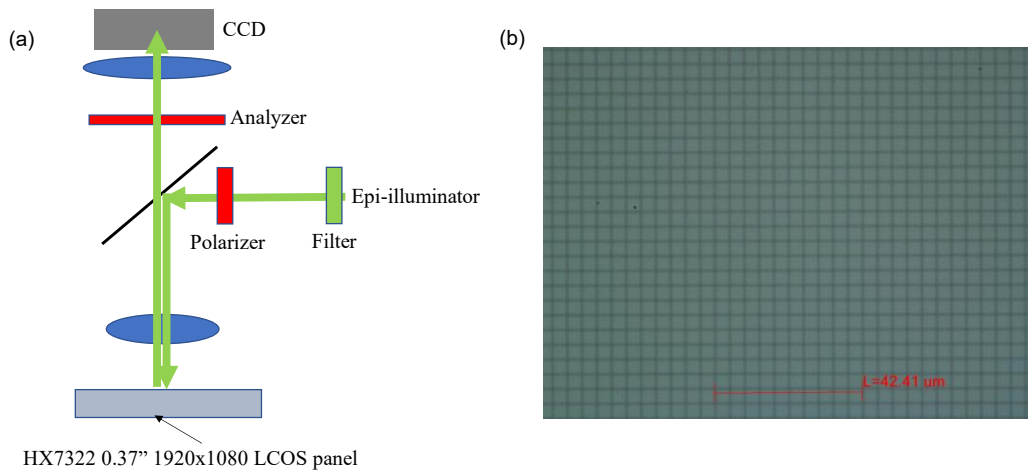
**Figure 5-4** Position-dependent reflectance corresponding to shielding walls with three different heights. The pixel pitch of amplitude LCoS is  $3 \mu\text{m}$ .



**Figure 5-5** The position-dependent normalized reflectance with linearly polarized and circularly polarized light corresponding to (a) without shielding walls, and (b) with shielding walls. The pixel pitch is  $3 \mu\text{m}$ .

### 5.3 Experimental measurements

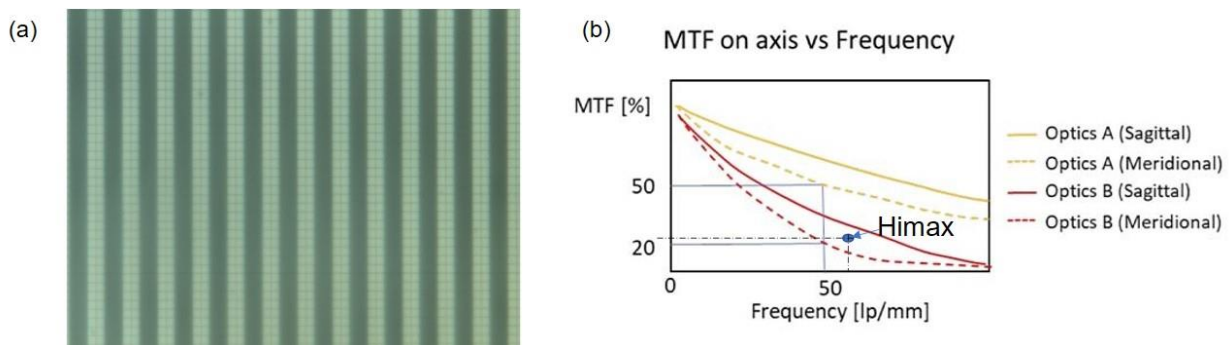
Although the FFE of VA mode has been experimentally reported in literatures, few experimental results on the FFE of MTN have been unveiled. To measure the FFE of the MTN LCoS panel, an experimental setup was established, as schematized in Figure 5-6(a). We inserted a green color filter and a polarizer after the external white illuminator to obtain linearly polarized green light. Before placing the LCoS panel on the microscope stage, we rotated the analyzer to obtain a minimum reflectance and thereby confirmed that the polarizer and analyzer were orthogonal. Then we placed the LCoS panel on the microscope stage and the light beam was reflected by the LCoS panel. The intensity distribution at the pixel level can be finally detected by the CCD camera. Figure 5-6(b) shows the observed fine pixel structure under the microscope. From the red scale bar, we can infer that the pixel pitch is  $4.24\ \mu\text{m}$ , which matches with the value Himax Technologies provides.



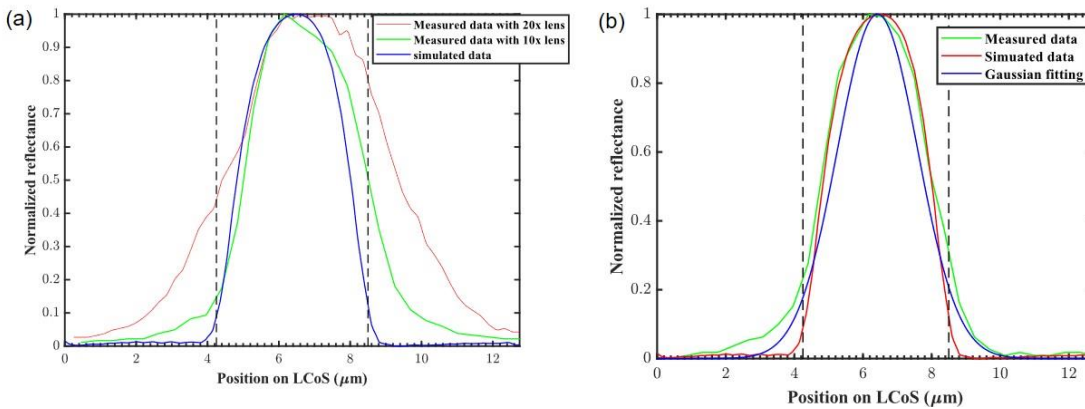
**Figure 5-6 (a) Schematic of the experimental setup for measuring the FFE (b) microscopy pixel structure of the MTN LCoS panel.**

Figure 5-7(a) shows a microscope image with a 40x objective lens. The input pattern is a series of white/black lines. The width of a white line is equal to that of two pixels. Therefore, the

spatial frequency of the input pattern is calculated to be 59 lp/mm (line pairs per millimeter). According to Figure 5-7(a), the measured contrast is 23%. Such a low contrast arises from not only the FFE but also mainly the resolving power of the objective lens. To evaluate the lens performance, modulation transfer function (MTF) can be used. Figure 5-7(b) depicts MTF curves of two optical systems, which refer to the website of Olympus microscopes [65]. The data extracted from Figure 5-7(a) is marked in Figure 5-7(b), demonstrating that the 40x objective lens used by Himax has a similar performance to optics B. A higher magnification objective lens usually has a larger NA value and larger aberrations. To mitigate the influence of MTF exerting on the experimental measurements of FFE, we employed a low magnification objective lens with a high f-number. For comparison, the experimental results using 20x and 10x objective lenses are shown in Figure 5-8(a). The measured data using the 20x objective lens show greater crosstalk than those using the 10x objective lens. To further bridge the gap between experimental results and simulation results, a bandpass filter with the central wavelength of 570 nm was inserted after the external white illuminator, as shown in Figure 5-8(b). From Figure 5-8(b), the measured data agree with simulated one, except a slight deviation at the edges of the middle pixel.



**Figure 5-7 (a) A microscopical image with a 40x objective lens provided by Himax (b) the frequency-dependent MTF [65] with a marked dot representing the data extracted from (a).**



**Figure 5-8 The position-dependent reflectance using (a) white light, and (b) green light.**

To mitigate the FFE of the measured LCoS panel, we collaborated with Himax to develop a MTN LCoS panel with a thinner cell gap. After we have received a new LCoS panel filled with JNC-5134, it is necessary to characterize it and compare it with the previous LCoS panel filled with Merck material. By simulating the FFE, [Figure 5-9](#) shows that the LCoS with JNC-5134 exhibits a higher optical efficiency and less crosstalk because the cell gap for JNC-5134 ( $d = 1.28 \mu\text{m}$ ) is smaller than that for Merck ( $d = 1.6 \mu\text{m}$ ). We also did experiments to verify that the crosstalk is mitigated in the new LCoS panel, as shown in [Figure 5-10](#). Light leakage is more pronounced in the 20x objective lens, which mainly arises from the aberrations of high magnification objective lens. After we experimentally verify that a thinner cell gap helps suppress the crosstalk, we simulate the FFE with 1.5- $\mu\text{m}$  pixel size at  $\beta = 0^\circ$ , corresponding to 0.7- $\mu\text{m}$  and 1- $\mu\text{m}$  cell gap, respectively. [Figure 5-11](#) shows that the 0.7- $\mu\text{m}$  cell gap helps reduce the FFE further, but the required birefringence is as high as 0.264 to achieve  $d\Delta n = 184.8 \text{ nm}$  at  $\lambda = 550 \text{ nm}$ , inevitably posing challenges to the material stability and low viscosity.

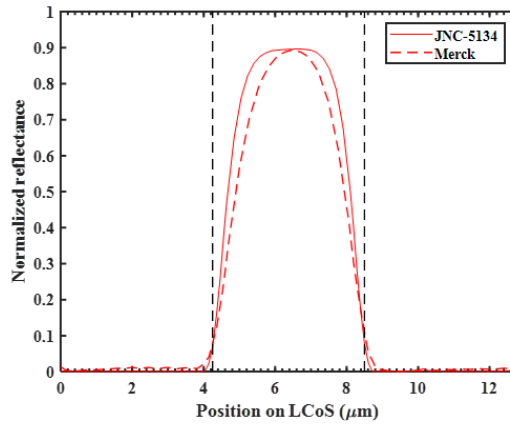


**Figure 5-9 Comparison of the simulated FFE between two LCoS panels filled with JNC-5134 and Merck LC mixture, respectively.**

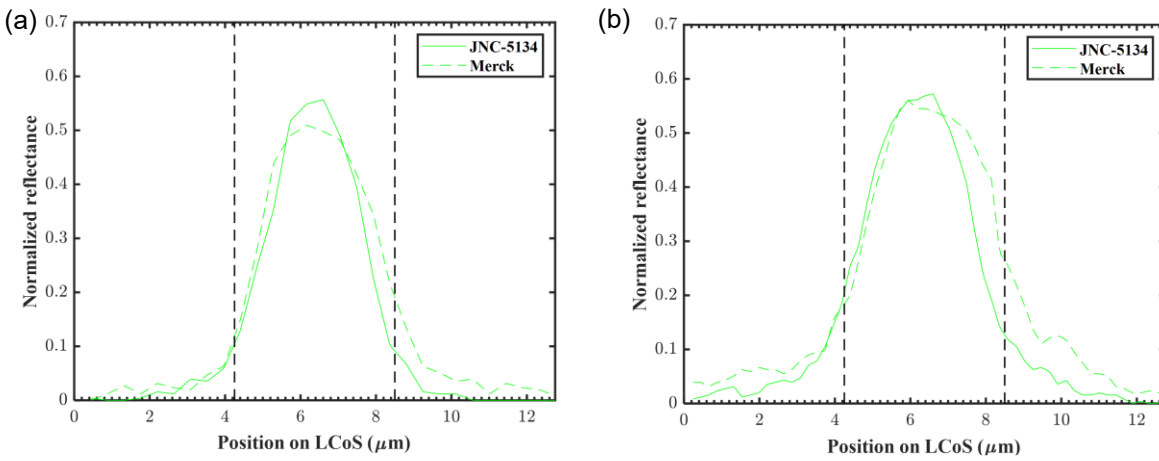


**Figure 5-10. Comparison of the measured FFE using a (a) 10x objective lens, and (b) 20x objective lens.**

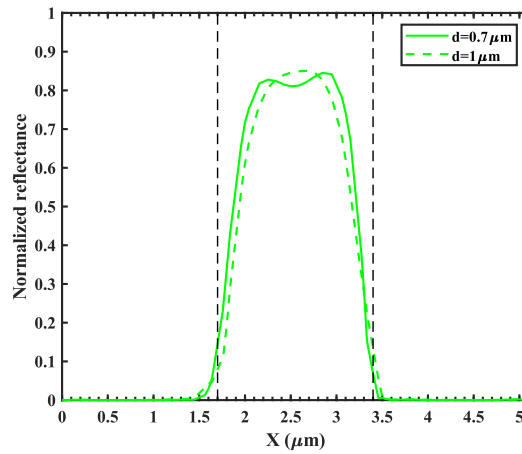


**Figure 5-11. Comparison of the simulated FFE corresponding to 0.7- $\mu\text{m}$  and 1- $\mu\text{m}$  cell gaps.**

#### 5.4 Summary

In this chapter, we report some interesting findings, such as the effect of incident polarization, anchoring energy, and  $\beta$  angle on the MTN mode. We also reveal the physical mechanism why a circularly polarized light leads to a greater crosstalk in the MTN LCoS. The optimal  $\beta$  angle may not be at  $20^\circ$  when the FFE plays a vital role in ultrasmall pixel-size LCoS panels. Dielectric walls are proven to be effective in improving the performance of MTN LCoS panel. As for measuring the FFE, we analyze some factors that impact our experimental results and compare them with simulation results. Lastly, we use experimental data to validate that the LCoS panel with a thinner cell gap exhibits a weaker FFE.

## CHAPTER 6: CONCLUSIONS

In this dissertation, we aim to developing next-generation high-performance virtual reality and augmented reality displays. To enhance the performance of display light engines, we propose novel measurement strategies and practical solutions such as field sequential color, progressive emission, high-order antinodes, and optimized alignment angle (thin cell gap). These emerging solutions will contribute to achieving high resolution density, high optical efficiency, wide color gamut, and small form factor for near-eye display systems.

Mini-LED backlit LCDs can help LCDs achieve high dynamic range and compete with OLED displays. Using quantitative measurement data, mini-LED backlit LCDs can exhibit a higher peak brightness, a more accurate gamma curve, and ambient contrast ratio. But OLED displays are halo-free, and mini-LED backlit LCDs exhibit annoying halo effect that needs to be carefully considered and compensated. The LMK with a high-resolution CMOS sensor was employed to characterize the halo effect and reconstruct the real luminance profiles. The confining reflector wall helps reduce the zone crosstalk and the halo effect. We also adopted a novel strategy to measure the point spread function of the backlight module. Such a systematic comparison and measurement can also extend to the comparison between Meta Quest 3 (adopting LCDs) and Apple Vision Pro (adopting micro-OLEDs) via considering the effect of imaging optics and more metrics such as the resolution density and motion blur. Also, a mini-LED backlight helps achieve progressive emission and thus enables a higher subframe rate for field sequential color LCDs.

In VR devices, high-resolution density is critical for eliminating screen-door effect and reproducing fine details. In Chapter 3, we propose an FSC LCD to triple the resolution density of

color filter-based LCDs while keeping a low power consumption for compact VR displays. To prove concept, in experiment we reported and evaluated a new high birefringence and low viscosity nematic LC mixture. Our simulation results show that the average GTG response time can be as fast as  $\sim 1.5$  ms. To further mitigate the CBU, we also propose progressive emission enabled by mini-LEDs to demonstrate a subframe rate of 600 Hz. Compared to simultaneous emission, the subframe rate is almost doubled. The FSC LCD also exhibits a high contrast ratio, superior color uniformity, and wide color gamut. Overall, our proposed and designed high-framerate FSC LCD exhibits potential to significantly advance VR display industry in the future.

As another type of VR light engine, micro-OLED exhibits a high-resolution density and small form factor. Current micro-OLED adopts white OLEDs and color filters because of a relatively easier manufacturing. Owing to the wide emission spectra and crosstalk of the employed color filters, the color gamut of WOLEDs is usually smaller than 100% DCI-P3. In Chapter 4, we propose a new structure to combine the high-order antinodes and the patterned microcavities to achieve an ultrawide color gamut. First, we model the micro-OLED and pancake optical system, serving as a basis for systematical analysis and optimization. For both B/YG and B/G/R WOLEDs, we first analyze the boundary constraints to speed up the simulation process, and then optimize their performances. At the optimal conditions, our proposed structure can improve the efficiency of B/YG WOLED by  $\sim 62\%$  compared to the B/YG WOLED with the low-order antinodes. For B/G/R WOLED, a color gamut of 95% Rec. 2020 can be achieved with a moderate microcavity.

For AR devices, the required resolution density and brightness are much higher than VR devices, which pose great challenges to micro-OLEDs. To solve these challenges, in Chapter 5,

we have developed a small pixel-size LCoS with a reduced FFE and mitigated lifetime issue, contributing to small form factor or high resolution. Some parameters such as the incident polarization, anchoring energy, and  $\beta$  angle are systematically investigated in the MTN LCoS. For example, a circularly polarized light leads to a greater crosstalk in the MTN LCoS. The optimal  $\beta$  angle may not be at  $20^\circ$  when the FFE plays a vital role in ultrasmall pixel-size LCoS panels. We can also leverage dielectric walls to improve the efficiency and reduce the crosstalk of the MTN LCoS. In addition to dielectric walls, a more straightforward method of suppressing the FFE is to employ a thinner cell gap, which has been validated by experimental data. We expect that such a high-performance LCoS will accelerate the widespread applications of AR glasses.

## **APPENDIX: STUDENT PUBLICATIONS**

### Journal publications

1. Y. Qian, **Z. Yang**, E.-L. Hsiang, Q. Yang, K. Nilsen, Y. H. Huang, K. H. Lin, and S. T. Wu, “Human Eye Contrast Sensitivity to Vehicle Displays under Strong Ambient Light,” *Crystals* **13**, 1384 (2023).
2. Y. Ding, Q. Yang, Y. Li, **Z. Yang**, Z. Wang, H. Liang, and S. T. Wu, “Waveguide-based augmented reality displays: perspectives and challenges,” *eLight* **3**, 24 (2023).
3. C. Lin, ...**Z. Yang**, et al., “The Micro-LED Roadmap: Status Quo and Prospects,” *J. Phys. Photon* **5**(4), 042502 (2023).
4. Y. Qian, **Z. Yang**, Y. H. Huang, K. H. Lin, and S. T. Wu, “High efficiency nanowire LEDs for AR and VR displays,” *J. Soc. Inf. Disp.* **31**(5), 336-343 (2023).
5. E. L. Hsiang, **Z. Yang**, and S. T. Wu, “Optimizing microdisplay requirements for pancake VR applications,” *J. Soc. Inf. Disp.* **31**(5), 264-273 (2023).
6. **Z. Yang**, Y. Qian, J. Zou, and S. T. Wu, “Reducing the power consumption of VR displays with a field sequential color LCD,” *Appl. Sci.* **13**, 2635 (2023).
7. Y. Qian, **Z. Yang**, Y. H. Huang, K. H. Lin, and S. T. Wu, “Directional high-efficiency nanowire LEDs with reduced angular color shift for AR and VR displays,” *Opto-Electronic Science*, **1**(12), 220021 (2022).
8. **(co-first author)** E. L. Hsiang, **Z. Yang**, Q. Yang, P.C. Lai, C.L. Lin, and S. T. Wu, “AR/VR light engines: perspectives and challenges,” *Adv. Opt. Photonics.* **14**, 783-861 (2022).

9. K. Yin, E. L. Hsiang, J. Zou, Y. Li, **Z. Yang**, Q. Yang, P.C. Lai, C.L. Lin, and S. T. Wu, “Advanced liquid crystal devices for augmented reality and virtual reality displays: Principles and Applications,” *Light Sci. Appl.* 11, 161 (2022).
10. Q. Yang, **Z. Yang**, Y.F. Lan, and S. T. Wu, “Low-diffraction transparent  $\mu$ LED displays with optimized pixel structure,” *J. Soc. Inf. Disp.* 30, 395-403 (2022).
11. **Z. Yang**, E. L. Hsiang, Y. Qian, and S. T. Wu, “Performance comparison between mini-LED backlit LCD and OLED display for 15.6-inch notebook computers,” *Appl. Sci.* 12, 1239 (2022).
12. E. L. Hsiang, **Z. Yang**, T. Zhan, J. Zou, H. Akimoto, and S. T. Wu, “Optimizing the display performance for virtual reality systems,” *Opt. Continuum* 4(12), 3052-3067 (2021).
13. E. L. Hsiang, Z. He, **Z. Yang**, Y. F. Lan, and S. T. Wu, “Tailoring the light distribution of micro-LED displays with a compact compound parabolic concentrator and an engineered diffusor,” *Opt. Express* 29(24), 39859-39873 (2021).
14. J. Zou, **Z. Yang**, C. Mao, and S. T. Wu, “Fast-Response Liquid Crystals for 6G Optical Communications,” *Crystals* 11, 797 (2021).
15. **(co-first author)** E. L. Hsiang, **Z. Yang**, Q. Yang, Y. F. Lan, and S. T. Wu, “Prospects and challenges of mini-LED, OLED, and micro-LED displays,” *J. Soc. Inf. Disp.* 29(6), 446-465 (2021).
16. **Z. Yang**, T. Zhan, and S. T. Wu, “Polarization independent liquid crystal-based refractive index sensor,” *J. Soc. Inf. Disp.* 29(5), 1-6 (2021).

17. Y. Li, T. Zhan, **Z. Yang**, C. Xu, P. L. LiKamWa, K. Li, and S. T. Wu, “Broadband cholesteric liquid crystal lens for chromatic aberration correction in catadioptric virtual reality optics,” *Opt. Express* 29(4), 6011-6020 (2021).
18. Y. Li, **Z. Yang**, R. Chen, L. Mo, J. Li, M. Hu, and S. T. Wu, “Submillisecond-response polymer network liquid crystal phase modulators,” *Polymers* 12, 2862 (2020).
19. **Z. Yang**, T. Zhan, and S. T. Wu, “Polarization independent guided-mode resonance in liquid crystal-based polarization gratings,” *Opt. Continuum* 3(11), 3107-3115 (2020).

Conference proceedings

1. **Z. Yang**, E. L. Hsiang, Y. Qian, and S. T. Wu, “Systematic Comparisons on Display Performances including Halo Effect,” SID Symp. Digest 53 (1), 436-439. (2022)
2. E. L. Hsiang, Z. He, **Z. Yang**, Y. F. Lan, and S. T. Wu, “High Efficiency  $\mu$ LED Light Engine for AR/VR Displays,” SID Symp. Digest 53 (1), 1316-1319. (2022)
3. Q. Yang, **Z. Yang**, Y.F. Lan, and S. T. Wu, “Low-Diffraction Transparent  $\mu$ LED Displays with Optimized Pixel Structure,” SID Symp. Digest 53 (1), 715-718. (2022)
4. E. L. Hsiang, **Z. Yang**, T. Zhan, J. Zou, H. Akimoto, and S. T. Wu, “Analysis and optimization on display performance for virtual reality,” Advances in Display Technologies XII 12024, 15-23. (2022)
5. **Z. Yang**, T. Zhan, and S. T. Wu, “Polarization-Independent liquid-Crystal-Based Refractive Index Sensor,” SID Symp. Digest 52 (1), 780-783. (2021)
6. Y. Li, T. Zhan, **Z. Yang**, C. Xu, P. L. LiKamWa, K. Li, and S. T. Wu, “Chromatic Aberration Correction Enabled by Broadband Cholesteric Liquid-Crystal Lens for Pancake Virtual-Reality Optics,” SID Symp. Digest 52 (1), 424-426. (2021)
7. Y. Qian, **Z. Yang**, Y. H. Huang, K. H. Lin, and S. T. Wu, “High Efficiency Nanowire LEDs for AR/VR displays”, SID Symp. Digest 54 (1), 144-147 (2023).
8. **Z. Yang**, Y. Qian, J. Zou, and S. T. Wu, “Field Sequential Color LCD for Enabling 60-PPD and 100°-FoV VR Displays”, SID Symp. Digest 54 (1), 749-752 (2023).
9. E. L. Hsiang, **Z. Yang**, and S. T. Wu, “Optimizing Microdisplay Requirements for Pancake VR applications”, SID Symp. Digest 54 (1), 386-389 (2023).

10. **Z. Yang**, Y. Qian, and S. T. Wu, “Emerging microdisplay technologies for AR/VR applications”, SID Symp. Digest 54 (1), 849-852 (2023).

## REFERENCES

1. A. Maimone and J. Wang, "Holographic optics for thin and lightweight virtual reality," *ACM Trans. Graph.* **39**, 67 (2020).
2. Q. Yang, Z. Yang, Y. F. Lan, and S. T. Wu, "Low-diffraction transparent micro light-emitting diode displays with optimized pixel structure," *J. Soc. Inf. Disp.* **30**, 395–403 (2022).
3. S. T. Wu and C. S. Wu, "Mixed-mode twisted nematic liquid crystal cells for reflective displays," *Appl. Phys. Lett.* **68**, 1455–1457 (1996).
4. D. Dudley, W. M. Duncan, and J. Slaughter, "Emerging digital micromirror device (DMD) applications," *Proc. SPIE* **4985**, 14–25 (2003).
5. A. P. Ghosh, "Full-color OLED on silicon microdisplay," *Proc. SPIE* **4464**, 1–10 (2002).
6. E. L. Hsiang, Z. He, Z. Yang, Y. F. Lan, and S. T. Wu, "P-74: Student Poster: High Efficiency  $\mu$ LED Light Engine for AR/VR Displays," *SID Symp. Dig. Tech. Pap.* **53**, 1316–1319 (2022).
7. Y. Qian, Z. Yang, Y. H. Huang, K. H. Lin, and S. T. Wu, "High-efficiency nanowire light-emitting diodes for augmented reality and virtual reality displays," *J. Soc. Inf. Disp.* **31**, 211–219 (2023).
8. F. Fidler, A. Balbekova, L. Noui, S. Anjou, T. Werner, and J. Reitterer, "Laser beam scanning in XR: benefits and challenges," *Proc. SPIE* **11765**, 1176502 (2021).
9. E. L. Hsiang, Z. Yang, Q. Yang, P. C. Lai, C. L. Lin, and S. T. Wu, "AR/VR light engines: perspectives and challenges," *Adv. Opt. Photon.* **14**, 783–861 (2022).

10. K. Yin, E. L. Hsiang, J. Zou, Y. Li, Z. Yang, Q. Yang, P. C. Lai, C. L. Lin, and S. T. Wu, "Advanced liquid crystal devices for augmented reality and virtual reality displays: principles and applications," *Light Sci. Appl.* **11**, 161 (2022).
11. Y. Qian, Z. Yang, Y. H. Huang, K. H. Lin, and S. T. Wu, "Directional high-efficiency nanowire LEDs with reduced angular color shift for AR and VR displays," *Opto-Electron. Sci.* **1**, 220021 (2022).
12. N. W. Melena and J. T. Wiersma, "Pixel size requirements for AR/MR," *Proc. SPIE* **11765**, 1176505 (2021).
13. X. B. Zhang, R. Wang, D. Dong, J. H. Han, and H. X. Wu, "Dynamic Backlight Adaptation Based on the Details of Image for Liquid Crystal Displays," *J. Disp. Technol.* **8**, 108–111 (2012).
14. H. Akimoto, A. Yamamoto, H. Washio, and T. Nakano, "46-3: Invited Paper: Design and Process of 2D Backlight Beyond HDR 5000 Nits," *SID Symp. Dig. Tech. Pap.* **52**, 628–631 (2021).
15. E. L. Hsiang, Q. Yang, Z. He, J. Zou, and S. T. Wu, "Halo effect in high-dynamic-range mini-LED backlit LCDs," *Opt. Express* **28**, 36822–36837 (2020).
16. J. H. Lee, C. H. Chen, P. H. Lee, H. Y. Lin, M. K. Leung, T. L. Chiu, and C. F. Lin, "Blue organic light-emitting diodes: current status, challenges, and future outlook," *J. Mater. Chem. C* **7**, 5874–5888 (2019).
17. Z. Yang, E. L. Hsiang, Y. Qian, and S. T. Wu, "Performance comparison between mini-LED backlit LCD and OLED display for 15.6-inch notebook computers," *Appl. Sci.* **12**, 1239 (2022).

18. E. Kim, J. Chung, J. Lee, H. Cho, N. S. Cho, and S. Yoo, "A systematic approach to reducing angular color shift in cavity-based organic light-emitting diodes," *Org. Electron.* **48**, 348–356 (2017).
19. F. Gou, E. L. Hsiang, G. Tan, P. T. Chou, Y. L. Li, Y. F. Lan, and S. T. Wu, "Angular color shift of micro-LED displays," *Opt. Express* **27**, A746 (2019).
20. Z. Yang, Y. Qian, J. Zou, and S. T. Wu, "52-3: Field sequential color LCD for enabling 60-PPD and 100°-FoV VR displays," *SID Symp. Dig. Tech. Pap.* **54**, 749–752 (2023).
21. T. Matsushima, S. Kimura, and S. Komura, "Fast response in-plane switching liquid crystal display mode optimized for high-resolution virtual-reality head-mounted display," *J. Soc. Inf. Disp.* **29**, 221–229 (2021).
22. Z. Yang, Y. Qian, J. Zou, C. L. Lee, C. L. Lin, and S. T. Wu, "Reducing the Power Consumption of VR Displays with a Field Sequential Color LCD," *Appl. Sci.* **13**, 2635 (2023).
23. Q. Guo, K. Yan, V. Chigrinov, H. Zhao, and M. Tribelsky, "Ferroelectric Liquid Crystals: Physics and Applications," *Crystals* **9**, 470 (2019).
24. L. Shi, A. K. Srivastava, A. Cheung, C. T. Hsieh, C. L. Hung, C. H. Lin, C. H. Lin, N. Sugiura, C. W. Kuo, V. G. Chigrinov, and H. S. Kwok, "Active matrix field sequential color electrically suppressed helix ferroelectric liquid crystal for high resolution displays," *J. Soc. Inf. Disp.* **26**, 325–332 (2018).
25. Y. Huang, H. Chen, G. Tan, H. Tobata, S. ichi Yamamoto, E. Okabe, Y. F. Lan, C. Y. Tsai, and S. T. Wu, "Optimized blue-phase liquid crystal for field-sequential-color displays," *Opt. Mater. Express* **7**, 641–650 (2017).

26. J. Zou, Z. Yang, C. Mao, and S. T. Wu, "Fast-Response Liquid Crystals for 6G Optical Communications," *Crystals* **11**, 797 (2021).
27. Y. Li, T. Zhan, Z. Yang, C. Xu, P. L. LiKamWa, K. Li, and S. T. Wu, "Broadband cholesteric liquid crystal lens for chromatic aberration correction in catadioptric virtual reality optics," *Opt. Express* **29**, 6011–6020 (2021).
28. I. Haller, "Thermodynamic and static properties of liquid crystals," *Prog. Solid State Chem.* **10**, 103–118 (1975).
29. S. T. Wu and C. S. Wu, "Rotational viscosity of nematic liquid crystals A critical examination of existing models," *Liq. Cryst.* **8**, 171–182 (1990).
30. S. T. Wu, A. M. Lackner, and U. Efron, "Optimal operation temperature of liquid crystal modulators," *Appl. Opt.* **26**, 3441–3445 (1987).
31. H. Chen, F. Peng, Z. Luo, D. Xu, S. T. Wu, M. C. Li, S. L. Lee, and W. C. Tsai, "High performance liquid crystal displays with a low dielectric constant material," *Opt. Mater. Express* **4**, 2262–2273 (2014).
32. J. Rouf Talukder, Y. Huang, and S. T. Wu, "High performance LCD for augmented reality and virtual reality displays," *Liq. Cryst.* **46**, 920–929 (2019).
33. S. T. Wu, "Birefringence dispersions of liquid crystals," *Phys. Rev. A* **33**, 1270–1274 (1986).
34. T. H. Choi, J. H. Woo, Y. Choi, and T. H. Yoon, "Interdigitated pixel electrodes with alternating tilts for fast fringe-field switching of liquid crystals," *Opt. Express* **24**, 27569–27576 (2016).

35. T. H. Choi, S. W. Oh, Y. J. Park, Y. Choi, and T. H. Yoon, "Fast fringe-field switching of a liquid crystal cell by two-dimensional confinement with virtual walls," *Sci Rep* **6**, 27936 (2016).
36. C. L. Yang, Y. H. Wu, I. A. Yao, Y. S. Tsou, C. H. Tsai, and J. S. Lin, "47-1: Invited Paper: High Resolution HDR VR display using Mini-LED," *SID Symp. Dig. Tech. Pap.* **52**, 636–639 (2021).
37. G. Harbers and C. Hoelen, "LP-2: High Performance LCD Backlighting using High Intensity Red, Green and Blue Light Emitting Diodes," *SID Symp. Dig. Tech. Pap.* **32**, 702–705 (2001).
38. E. L. Hsiang, Z. Yang, Q. Yang, Y. F. Lan, and S. T. Wu, "Prospects and challenges of mini-LED, OLED, and micro-LED displays," *J. Soc. Inf. Disp.* **29**, 446–465 (2021).
39. C. Y. Wu, T. F. Wu, J. R. Tsai, Y. M. Chen, and C. C. Chen, "Multistring LED Backlight Driving System for LCD Panels With Color Sequential Display and Area Control," *IEEE Trans Ind Electron* **55**, 3791–3800 (2008).
40. Y. Motoyama, K. Sugiyama, H. Tanaka, H. Tsuchioka, K. Matsusaki, and H. Fukumoto, "High-efficiency OLED microdisplay with microlens array," *J. Soc. Inf. Disp.* **27**, 354–360 (2019).
41. P. Xiao, J. Huang, Y. Yu, and B. Liu, "Recent Developments in Tandem White Organic Light-Emitting Diodes," *Molecules* **24**, 151 (2019).
42. L. S. Liao, K. P. Klubek, and C. W. Tang, "High-efficiency tandem organic light-emitting diodes," *Appl. Phys. Lett.* **84**, 167–169 (2004).

43. Y. Chen and D. Ma, "Organic semiconductor heterojunctions as charge generation layers and their application in tandem organic light-emitting diodes for high power efficiency," *J. Mater. Chem.* **22**, 18718–18734 (2012).
44. H. W. Bae, Y. W. Kwon, M. An, J. Kim, J. H. Kwon, and D. Lee, "High-Color-Stability and Low-Driving-Voltage White Organic Light-Emitting Diodes on Silicon with Interlayers of Thin Charge Generation Units for Microdisplay Applications," *ACS Appl. Electron. Mater.* **3**, 3240–3246 (2021).
45. "KOPIN CORPORATION'S OLED MICRODISPLAY SUCCESS HIGHLIGHTED IN INDUSTRY RESEARCH," <https://www.kopin.com/press-releases/kopin-corporations-oled-microdisplay-success-highlighted-in-industry-research/>.
46. H. Cho, C. W. Byun, C. M. Kang, J. W. Shin, B. H. Kwon, S. Choi, N. S. Cho, J. I. Lee, H. Kim, J. H. Lee, M. Kim, and H. Lee, "White organic light-emitting diode (OLED) microdisplay with a tandem structure," *J. Inf. Disp.* **20**, 249–255 (2019).
47. W. Song, J. You, C. Y. Wu, L. Wang, Y. Shen, B. Bo, W. Quan, C. Luo, D. Yu, W. Li, H. T. Shih, and Z. Wu, "5-3: 3-Stacked Top-Emitting White OLEDs with Super-Wide Color Gamut and High Efficiency," *SID Symp. Dig. Tech. Pap.* **50**, 46–49 (2019).
48. S. J. Zou, X. Y. Zeng, Y. Q. Li, and J. X. Tang, "The Strategies for High-Performance Single-Emissive-Layer White Organic Light-Emitting Diodes," *Laser Photon. Rev.* **15**, 2000474 (2021).
49. J. Hamer, M. Kondakova, J. Spindler, R. Cupello, S. Hamer, M. Andre, S. McClurg, A. Pleten, B. Primerano, D. Scott, G. Scherer, and S. Stickel, "High-performance OLED

- microdisplays made with multi-stack OLED formulations on CMOS backplanes," *Proc. SPIE* **11473**, 114730F (2020).
50. Y. Qian, Z. Yang, E. L. Hsiang, Q. Yang, K. Nilsen, Y. H. Huang, K. H. Lin, and S. T. Wu, "Human Eye Contrast Sensitivity to Vehicle Displays under Strong Ambient Light," *Crystals* **13**, 1384 (2023).
51. E. L. Hsiang, Z. Yang, T. Zhan, J. Zou, H. Akimoto, and S. T. Wu, "Optimizing the display performance for virtual reality systems," *OSA Contin.* **4**, 3052–3067 (2021).
52. E. L. Hsiang, Z. Yang, and S. T. Wu, "Optimizing microdisplay requirements for pancake VR applications," *J. Soc. Inf. Disp.* **31**, 264–273 (2023).
53. S. K. Kim, M. J. Park, R. Lampande, S. W. Jung, H. un Park, J. K. Jeong, and J. H. Kwon, "Primary color generation from white organic light-emitting diodes using a cavity control layer for AR/VR applications," *Org. Electron.* **87**, 105938 (2020).
54. E. L. Hsiang, Z. Yang, T. Zhan, J. Zou, H. Akimoto, and S. T. Wu, "Analysis and optimization on display performance for virtual reality," *Proc. SPIE* **12024**, 1202405 (2022).
55. Y. Ding, Q. Yang, Y. Li, Z. Yang, Z. Wang, H. Liang, and S. T. Wu, "Waveguide-based augmented reality displays: perspectives and challenges," *eLight* **3**, 24 (2023).
56. Z. Yang, Y. Qian, and S. T. Wu, "60-1: Invited Paper: Emerging microdisplay technologies for AR/VR applications," *SID Symp. Dig. Tech. Pap.* **54**, 849–852 (2023).
57. E. L. Hsiang, Z. He, Z. Yang, Y. F. Lan, and S. T. Wu, "Tailoring the light distribution of micro-LED displays with a compact compound parabolic concentrator and an engineered diffusor," *Opt. Express* **29**, 39859–39873 (2021).

58. C. C. Lin, Y. R. Wu, H. C. Kuo, M. S. Wong, S. P. DenBaars, S. Nakamura, A. Pandey, Z. Mi, P. Tian, K. Ohkawa, D. Iida, T. Wang, Y. Cai, J. Bai, Z. Yang, Y. Qian, S. T. Wu, J. Han, C. Chen, Z. Liu, B. R. Hyun, J. H. Kim, B. Jang, H. D. Kim, H. J. Lee, Y. T. Liu, Y. H. Lai, Y. L. Li, W. Meng, H. Shen, B. Liu, X. Wang, K. ling Liang, C. J. Luo, and Y. H. Fang, "The micro-LED roadmap: status quo and prospects," *J. Phys. Photonics* **5**, 042502 (2023).
59. Z. Yang, T. Zhan, and S. T. Wu, "Polarization-independent liquid crystal-based refractive index sensor," *J. Soc. Inf. Disp.* **29**, 305–310 (2021).
60. Z. Yang, T. Zhan, and S. T. Wu, "Polarization independent guided-mode resonance in liquid crystal-based polarization gratings," *OSA Contin.* **3**, 3107–3115 (2020).
61. Y. Li, Z. Yang, R. Chen, L. Mo, J. Li, M. Hu, and S. T. Wu, "Submillisecond-Response Polymer Network Liquid Crystal Phase Modulators," *Polymers* **12**, 2862 (2020).
62. K. H. Fan Chiang, S. T. Wu, and S. H. Chen, "Fringing Field Effect of the Liquid-Crystal-on-Silicon Devices," *Jpn. J. Appl. Phys.* **41**, 4577–4585 (2002).
63. K. H. Fan Chiang, S. H. Chen, and S. T. Wu, "High-definition vertically aligned liquid crystal microdisplays using a circularly polarized light," *Appl. Phys. Lett.* **87**, 031110 (2005).
64. Y. Isomae, Y. Shibata, T. Ishinabe, and H. Fujikake, "Design of 1- $\mu$ m-pitch liquid crystal spatial light modulators having dielectric shield wall structure for holographic display with wide field of view," *Opt. Rev.* **24**, 165–176 (2017).
65. "What Is the Modulation Transfer Function?," <https://www.olympus-lifescience.com/en/resources/white-papers/what-is-the-modulation-transfer-function/>.